

## MIT Open Access Articles

*Observations of ion-neutral coupling associated  
with strong electrodynamic disturbances  
during the 2015 St. Patrick's Day storm*

The MIT Faculty has made this article openly available. **Please share**  
how this access benefits you. Your story matters.

**Citation:** Zhang, Shun-Rong et al. "Observations of Ion-Neutral Coupling Associated with Strong Electrodynamic Disturbances During the 2015 St. Patrick's Day Storm." *Journal of Geophysical Research: Space Physics* 122, 1 (January 2017): 1314–1337 © 2017 American Geophysical Union

**As Published:** <http://dx.doi.org/10.1002/2016JA023307>

**Publisher:** American Geophysical Union (AGU)

**Persistent URL:** <http://hdl.handle.net/1721.1/113630>

**Version:** Final published version: final published article, as it appeared in a journal, conference proceedings, or other formally published context

**Terms of Use:** Article is made available in accordance with the publisher's policy and may be subject to US copyright law. Please refer to the publisher's site for terms of use.



## RESEARCH ARTICLE

10.1002/2016JA023307

## Special Section:

Geospace system responses to the St. Patrick's Day storms in 2013 and 2015

## Key Points:

- Multiple strong ion-neutral coupling effects appeared within a few hours of SAPS during a single intensification of a great magnetic storm
- Strong ion-neutral frictional heating accompanied by large atmospheric upwelling, with ion upwelling as a potential source of ion upflow
- Oscillating electric fields accompanied large scale storm time traveling atmospheric disturbances

## Correspondence to:

S.-R. Zhang,  
shunrong@haystack.mit.edu

## Citation:

Zhang, S.-R., P. J. Erickson, Y. Zhang, W. Wang, C. Huang, A. J. Coster, J. M. Holt, J. F. Foster, M. Sulzer, and R. Kerr (2017), Observations of ion-neutral coupling associated with strong electrodynamic disturbances during the 2015 St. Patrick's Day storm, *J. Geophys. Res. Space Physics*, 122, doi:10.1002/2016JA023307.

Received 10 AUG 2016

Accepted 30 DEC 2016

Accepted article online 2 JAN 2017

## Observations of ion-neutral coupling associated with strong electrodynamic disturbances during the 2015 St. Patrick's Day storm

Shun-Rong Zhang<sup>1</sup> , Philip J. Erickson<sup>1</sup> , Yongliang Zhang<sup>2</sup> , Wenbin Wang<sup>3</sup> , Chaosong Huang<sup>4</sup> , Anthea J. Coster<sup>1</sup> , John M. Holt<sup>1</sup>, John F. Foster<sup>1</sup> , Michael Sulzer<sup>5</sup>, and Robert Kerr<sup>6</sup> 
<sup>1</sup>Haystack Observatory, Massachusetts Institute of Technology, Westford, Massachusetts, USA, <sup>2</sup>Applied Physics Laboratory, The Johns Hopkins University, Baltimore, Maryland, USA, <sup>3</sup>High Altitude Observatory, National Center for Atmospheric Research, Boulder, Colorado, USA, <sup>4</sup>Air Force Research Laboratory, Wright-Patterson, Ohio, USA, <sup>5</sup>Arecibo Observatory, SRI International, Menlo Park, California, USA, <sup>6</sup>Computational Physics, Inc., Springfield, Virginia, USA

**Abstract** We use incoherent scatter radar observations at Millstone Hill (MHO) and Arecibo (AO) and topside ionosphere in situ Defense Meteorological Satellite Program (DMSP) observations during the great geomagnetic storm on 17–18 March 2015 to conduct a focused study on ion-neutral coupling and storm time ionosphere and thermosphere dynamics. Some of these observations were made around the time of large ionospheric drifts within a subauroral polarization stream (SAPS). During the storm main phase, we identify multiple disturbance characteristics in the North American late afternoon and dusk sector. (1) Strong subauroral westward drifts occurred between 20 and 24 UT near MHO, accompanied by a storm enhanced density plume passage over MHO in the afternoon with a poleward/upward ion drift. The strongly westward flow reached 2000 m/s speed near the poleward plume edge. (2) Prompt penetration electric field signatures, appearing as poleward/upward ion drifts on the dayside over both MHO and AO, were consistent with DMSP vertical drift data and contributed to plume development. (3) Meridional wind equatorward surges occurred during daytime hours at MHO, followed by 2–3 h period oscillations at both MHO and AO. The zonal electric field at AO was strongly correlated with the wind oscillation. (4) Large ion temperature enhancements as well as 50+ m/s upward ion drifts throughout the *E* and *F* regions were observed during the SAPS period. These were presumably caused by strong frictional heating due to large plasma drifts. The heating effects appeared to drive significant atmospheric upwelling, and corresponding ion upflow was also observed briefly. This study highlights some of the important effects of fast plasma transport as well as other disturbance dynamics on ion-neutral coupling during a single intensification period within a great geomagnetic storm.

## 1. Introduction

The Earth's upper atmosphere responds to geospace storms in very complicated ways as charged particles in the ionosphere and neutral species in the thermosphere undergo dramatic electromagnetic, thermodynamic, and chemical changes. Identifying characteristic patterns of storm time ionosphere and thermosphere perturbations and understanding drivers causing these perturbations are essential topics under extensive community investigation for many decades. Reviews of some of these efforts can be found in *Buonsanto* [1999] and *Mendillo* [2006].

Renewed interest in storm time dynamics, especially over subauroral and midlatitudes as well as low and equatorial latitudes, has led to significant advances in the last decade. Notable milestones include characterization of the subauroral polarization stream (SAPS), [Foster and Burke, 2002], involving narrower features also known as subauroral ion drifts (SAID) and polarization jets (PJ) [Galperin et al., 1974; Spiro et al., 1979], and the SAPS role in the development of storm-enhanced density (SED) features at subauroral and midlatitudes [Foster, 1993]. Another area of renewed interest [Huang et al., 2006] involves improved understanding of penetrating electric fields [Nishida, 1968] from middle to equatorial latitudes and its relative importance to the storm time dynamo, generated during the equatorward propagation of atmospheric disturbances

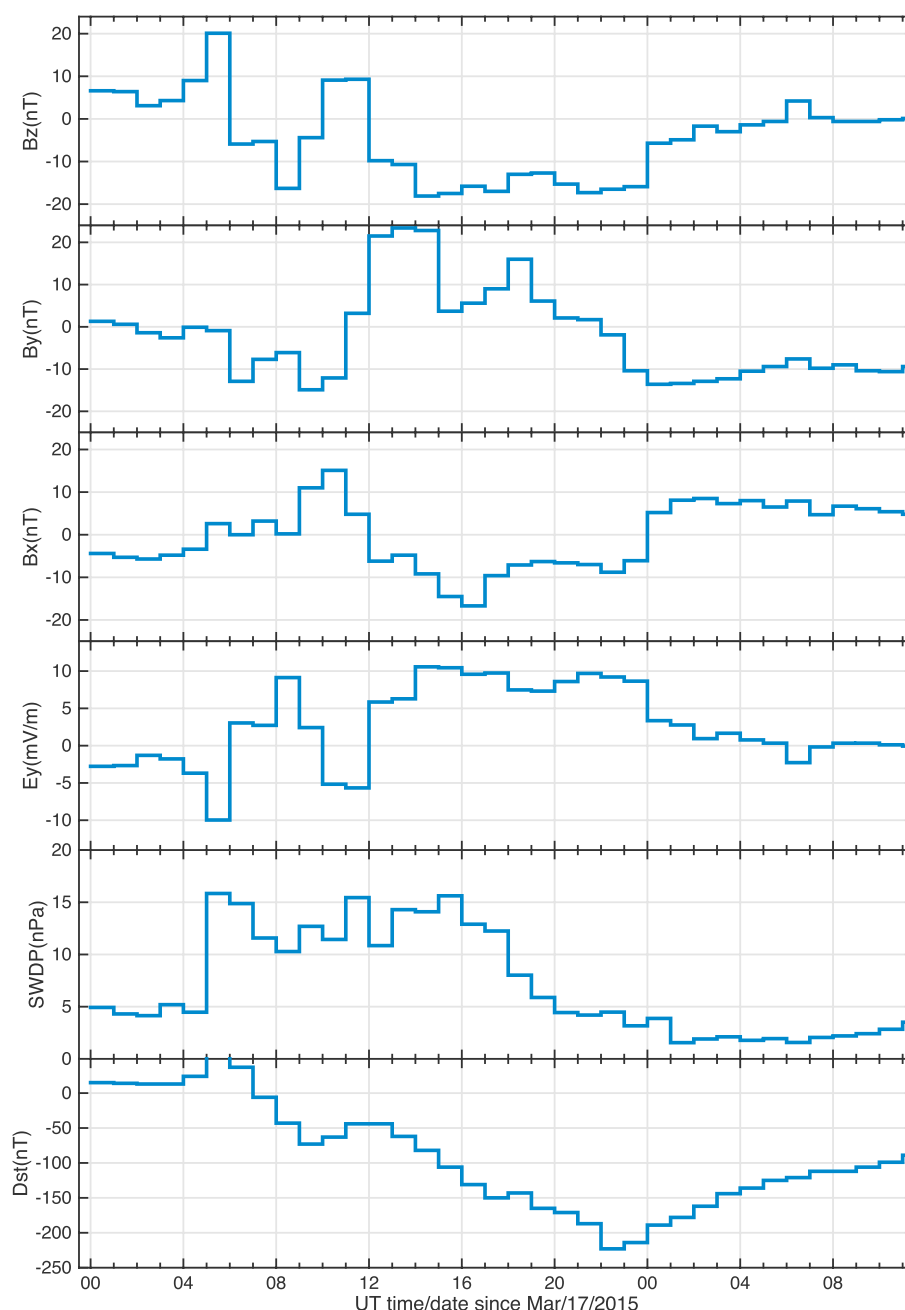


**Figure 1.** Solar geophysical conditions for 17–18 March 2015. (first three panels) IMF  $B_z$ ,  $B_y$  and  $B_x$  (all nT) in GSM coordinates; (fourth panel) interplanetary electric field dawn-to-dusk component  $E_y$  (mV/m) calculated as  $-B_z \times V_{sw}$  ( $V_{sw}$ , solar wind speed); (fifth panel) solar wind dynamic pressure SWDP (nPa); and (sixth panel) Dst index.

[Blanc and Richmond, 1980; Maruyama et al., 2005]. These achievements have been reached through joint observational and modeling efforts, with a key factor being recent enhanced capabilities for geospace observational networks with high fidelity spatial and temporal detection of ionospheric disturbances. It is important to point out that information regarding ionospheric and thermospheric dynamics is by definition incomplete without ion drift, neutral winds, and neutral composition in order to establish important physical links between electron density variations and their drivers. Observations of these important drivers are still quite few in general. However, a coordinated observational campaign conducted during the large 17–18 March 2015 St. Patrick's Day storm offers a rare opportunity to investigate important geophysical drivers and their storm time behavior during this great solar-terrestrial disturbance.

Great geomagnetic storms starting on 17 March 2015 were caused by joint effects of an arriving coronal mass ejection cloud and coronal hole high-speed streams [Kataoka *et al.*, 2015]. The event was characterized by a long (12 h) and intense ( $-18$  nT) southward interplanetary magnetic field (Figure 1), high  $K_p$  (8–) [Zhang *et al.*, 2015] and low  $Dst$  values (minimum  $-227$  nT). The storm on the 17th is the largest to date during solar cycle 24. Ionosphere and thermosphere responses to this storm have been the focus of recent community research (S.-R. Zhang *et al.*, CEDAR workshop, 2015; S.-R. Zhang *et al.*, AGU Fall Meeting, 2015) and this journal's special section. For example, Zhang *et al.* [2015] reported a large premidnight poleward thermospheric wind surge at subauroral and midlatitudes, in a direction opposite to the classical pattern of a storm time equatorward wind surge. The observed neutral wind variations were identified as driven by SAPS ion motions, through a scenario where strong ion flows cause a westward neutral wind and subsequently establish a poleward wind surge due to the Coriolis force on that westward wind. Liu *et al.* [2016] indicated that the associated SED plume observed in the Millstone Hill vicinity during the event was formed mostly in the topside ionosphere, and the  $F_2$  peak was in negative storm phase due to the arrival of a neutral atmospheric depression in the O/N<sub>2</sub> ratio. Other studies for this storm to date have examined global scale features of electron density variations and corresponding neutral O/N<sub>2</sub> changes as measured by multiple satellites [Astafyeva *et al.*, 2015], middle- and low-latitude ionospheric electron density variations as seen by GPS and ionosondes, and identification of the prompt penetration electric field (PPEF) and disturbance dynamo electric field (DDEF) using magnetometer data [Nava *et al.*, 2016]. Equatorial  $F_2$  region dynamics associated with PPEF and DDEF and other processes were reported in Tulasi Ram *et al.* [2016].

This paper addresses 17–18 March 2015 St. Patrick's Day storm-induced ionosphere and thermosphere disturbances in ionospheric plasma drifts (electric fields), neutral winds, and plasma temperatures, as observed at storm time subauroral latitudes (Millstone Hill, 42.6°N, 71.5°W, Invariant latitude 52.8°N) and lower midlatitudes (Arecibo, 13.8°N, 66.75°W, Invariant latitude 30.0°N). Observations here focus primarily on incoherent scatter radar (ISR) observations of ionospheric dynamics and also Fabry-Perot Interferometer (FPI) observations of neutral dynamics, along with in situ 840 km altitude topside ionospheric observations from the Defense Meteorological Satellite Program (DMSP) satellite constellation. Using data during this single intense storm event, we are able to comprehensively and simultaneously examine several SAPS related ion-neutral coupling topics: (1) meridional and zonal electric field intensifications (appearing in corresponding resolved plasma drift components), and their impact on subauroral and high latitude ionospheric plasma densities; (2) SAPS and penetration electric fields occurring during the same event at nearly the same time; (3) neutral meridional wind disturbances at Millstone Hill, some of which are related to SAPS flows; and (4) frictional heating effects throughout the  $E$  and  $F$  regions, through evidence of both neutral atmosphere and ionosphere upwelling as potential sources of ion upflow. The appearance of all these features in a single storm time event is unprecedented and provides a unique opportunity for advances in understanding of geospace dynamic processes associated with large plasma drifts. While the main theme of this study is effects that are highly associated with large ionospheric drifts (SAPS), this paper also discusses other storm time ionospheric and thermospheric disturbances and waves that were observed at subauroral and middle latitudes, but whose cause may or may not be related to SAPS flows.

## 2. Solar Geophysical Conditions and Ionospheric Observations

### 2.1. Solar Geophysical Conditions

The data used in this study were acquired during an international observational campaign alert window [Zhang *et al.*, 2015], and multiple ISR facilities were triggered to begin operations at  $\sim 15$  UT 17 March 2015, approximately 9 h into storm commencement. Both Millstone Hill and Arecibo ISRs conducted experiments for  $\sim 5$  days, but discussion here focuses primarily on the period from 20 to 24 UT on 17 March 2015 when strong plasma drift/electric field disturbances took place. Data surrounding the period and during relatively quiet conditions are also used to provide appropriate context.

The geospace storm was triggered by combined CME and high-speed stream effects. Severe geomagnetic disturbances occurred for an extended period with sudden commencement early on 17 March 2015 and recovery beginning early in the next day (Figure 1). Interplanetary magnetic field (IMF) northward component  $B_z$  hourly values in geocentric solar magnetospheric (GSM) coordinates fell to  $-17$  nT between 05 and 08 UT. Solar wind dynamic pressure was enhanced immediately and remained for  $\sim 12$  h at  $> 10$  nPa.  $B_z$  subsequently underwent a 12 h long sustained negative excursion of  $\sim -17$  nT between 12 and 24 UT on the 17th. During this main phase storm stage, IMF polarity was briefly "toward," then "away" for 12 h, and became toward

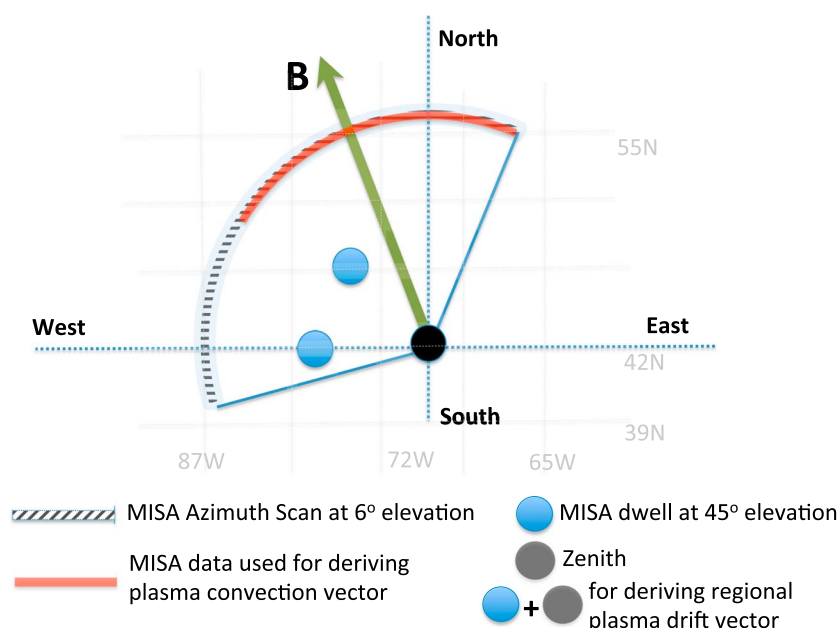


**Figure 2.** Millstone Hill ISR observational geometry of the radio beams viewed at the 300 km horizontal plane. The red arc represents data locations from the MISA azimuth scans at 6° elevation used for plasma convection velocity determination, and the three full circles represent data locations used for regional plasma velocity (and the *F* region meridional wind) determination. See text for details.

during the recovery phase on the 18th. The hourly *Dst* index dropped to a minimum of  $-227$  nT at 23 UT on the 17th. The interplanetary electric field (IEF) dawn-to-dusk component  $E_y$ , which is potentially linked to the low and middle-latitude penetration electric field [e.g., *Fejer et al.*, 1979; *Kelley et al.*, 2003; *Tsurutani et al.*, 2004; *Huang et al.*, 2006; *Basu et al.*, 2007], exhibited some fluctuations with maxima close to 10 mV/m around 14–16 UT and 21–24 UT. Ionospheric observations during these time frames indicate clear signatures of penetration electric fields (as discussed later in section 3.2). Interestingly, strong westward plasma flows in a SAPS configuration occurred during 20–24 UT, and its characteristics and impacts will be discussed throughout the paper.

## 2.2. Millstone Hill Observation and Data Processing

The Millstone Hill incoherent scatter radar has a long history of extensive auroral, subauroral, and midlatitude ionospheric observations using the 68 m diameter fixed zenith antenna as well as the 46 m full steerable MISA antenna [*Yeh et al.*, 1991; *Buonsanto et al.*, 1992; *Buonsanto and Foster*, 1993; *Foster et al.*, 2005; *Goncharenko et al.*, 2007; *Zhang and Holt*, 2007; *Zhang et al.*, 2007]. However, some of the data processing procedures used in this study, in particular, those producing ion drift vectors (electric fields) along with neutral wind processing, are not described elsewhere, and therefore a brief discussion is in order.

### 2.2.1. MHO Observation Mode

The ISR experiment executed at Millstone Hill was designed to provide wide coverage scans covering longitudes both east and west of Millstone Hill. This feature allowed observation of *F* region ionospheric conditions in the range of approximately  $-85$  to  $-65^\circ$ E longitude (at 250–300 km altitude). See Figure 2 for an observational geometry of the radar beams intersecting the horizontal plane at 300 km altitude. MISA steerable antenna scanning occurred from  $+20$  to  $-100^\circ$  azimuth (angle from geographic north) at a fixed elevation of  $6.0^\circ$ . The experiment paused scan sweeps at  $-55^\circ$  azimuth for a 240 s fixed dwell at  $45^\circ$  elevation. An interleaved 480  $\mu$ s waveform envelope sequence with both single/uncoded pulses (S/P; fundamental resolution = 64 km range) and alternating code (A/C; fundamental resolution = 4.5 km range) measurements [*Lehtinen and Häggström*, 1987] was used for a 180 s zenith profile at three intervals when the MISA was moving back to scan start, from scan end to west dwell, and west dwell to north dwell, respectively. The same interleaved S/P and A/C measurement sequence was also used at MISA fixed dwell positions of  $-90^\circ$  and  $0^\circ$  azimuth at  $45^\circ$  elevation, with all dwell durations 180 s except for the midazimuth scan fixed dwell. Total experiment cycle time for scans and fixed position dwells was  $\sim 37$  min.

### 2.2.2. Convection Plasma Velocity Vector (From Wide Coverage Scans)

The  $F$  region plasma drift vector may be expressed as different components in a geomagnetic coordinate system. We define these here as (1)  $V_{\text{per}E} \mathbf{E}_m \times \mathbf{B}/B^2$ , the drift perpendicular to the magnetic field and in the magnetic eastward direction, caused by  $\mathbf{E}_m$ , the meridional (equatorward) electric field perpendicular to the magnetic field; (2)  $V_{\text{per}N} \mathbf{E}_z \times \mathbf{B}/B^2$ , the drift perpendicular to the magnetic field and in the magnetic northward direction, and produced by  $\mathbf{E}_z$  the zonal (eastward) electric field perpendicular to the magnetic field; and (3)  $V_{\text{par}}$ , the field-aligned plasma drift (positive upward). These components cannot be measured simultaneously from a single monostatic radar. However, under the assumption of some measure of temporal and spatial stationarity, they can be determined from sequences of monostatic observations by combining line-of-sight ( $los$ ) velocity data from different scan positions within certain time and altitude bins. In particular, the vertical ion drift  $V_z$  can be directly measured by the zenith antenna and is equal to the  $los$  velocity. Therefore,

$$V_z = V_{\text{par}} \sin I + V_{\text{per}N} \cos I \quad (1)$$

$$V_{\text{par}} = V_d - U_n \cos I, \quad (2)$$

where  $V_d$  is the ambipolar diffusion velocity,  $I$  is the dip angle ( $\sim 67.5^\circ$  for the  $F$  region observations here), and  $U_n$  is the northward neutral wind in magnetic meridian.  $U_n$  may be expressed as  $U_n = U_N \cos D + U_E \sin D$ , where  $U_N$  and  $U_E$  are northward and eastward winds in geographic coordinates and  $D$  is magnetic declination ( $\sim -13.7^\circ$  in the  $F$  region).

For the ion convection velocity  $V_{\text{per}E}$ , we used  $los$  data within 1 h between  $-60$  and  $+10^\circ$  azimuth and 300–450 km altitude at  $6.0^\circ$  elevation. These look directions cover regions on east and west sides of the magnetic meridian plane within roughly a  $\pm 4^\circ$  (latitude) by  $\pm 10^\circ$  (longitude) bin, with mean location at geodetic coordinates of ( $51.4^\circ\text{N}$ ,  $86.7^\circ\text{W}$ ), and therefore sensitive to  $V_{\text{per}E}$ .  $V_{\text{per}N}$  is determined from the geometric feature that  $los$  is close to perpendicular to the field line near the magnetic meridian at the  $F$  region (the direction cosine in northward perpendicular to the field line is limited to 0.3), and the mean location determined from the 48–56° latitude bin is close to ( $51.1^\circ\text{N}$ ,  $86.0^\circ\text{W}$ ). These arrangements, which treat the two vector components slightly differently, allow for vector determination in geophysically interesting regions with reliable accuracy and small uncertainty. We assume here that the electric field does not change in time and space within each of the corresponding  $los$  bins over the joint measurement time. These bin sizes are either larger or comparable to a typical SAPS spatial scale ( $\sim 2$ – $5^\circ$  latitude width) and therefore encompass the complete SAPS spatial structure if it does occur. However, depending on the exact spatial and temporal distribution of the plasma drift, these resolved  $V_{\text{per}E}$  and  $V_{\text{per}N}$  represent SAPS features possibly mixed with other storm time subauroral and auroral plasma drift variations. Notice that the vectors derived in this manner are not local to Millstone Hill but occur about  $10^\circ$  to the north (for  $V_{\text{per}N}$ ) and  $10^\circ$  to the west (for  $V_{\text{per}E}$ ) of Millstone Hill.

The values of  $V_{\text{per}E}$  and  $V_{\text{per}N}$  produced by this binning and vector derivation process are used to demonstrate the plasma drift vector and the associated electric field at latitudes approximately  $10^\circ$  north/west of MHO (Figures 5a and 5b). In addition, the original spatial and temporal variation information for  $los$  is demonstrated in Figure 4 showing predominant temporal variations associated with large plasma drifts. These will be discussed in details in section 3.1.

### 2.2.3. $F$ Region Ion Velocity Vectors, Winds, and Gridded Data (Regional and Local Data)

To determine the three components of the plasma drift vector, a least squares fitting procedure was performed as part of the standard Millstone Hill Gridded Data product software package (profileFit). The resulting regridded radar data have a standard 15 min cadence and a set of standard altitudes with an altitude-dependent spacing. All local basic-derived parameter data regardless of waveform were processed, including data collected with beams pointed off zenith, and these results were used to estimate vector ion drift velocities. Low elevation ( $< 45^\circ$ ) data were excluded. Scalar data such as electron density and electron and ion temperature were then fit with a bicubic tensor product spline in time and altitude. If off-zenith velocity measurements were available, the procedure also estimated the electric field and vector ion drift. Measurements were assumed to be on the same magnetic field line which was assumed to be equipotential. In the  $F$  region, this reduced the measurement problem to a two parameter fit for the electric field at a reference altitude. Since the field lines are equipotentials, these two parameters define the electric field and ion  $\text{O}^+$  drift velocity at all  $F$  region altitudes. In the  $E$  region, the drifts are much more influenced by collisions with the neutral atmosphere, and a bicubic (time and height) spline was therefore used to model this component of the drift velocity.



Once the fits were computed, the gridded data were evaluated at the specified cadence and altitudes. Given the gridded basic derived parameter data, it is possible to compute other parameters of interest such as the meridional neutral wind. The profileFit package also facilitates calculation of height gradients in electron density  $N_e$ , ion temperature  $T_i$ , and electron temperature  $T_e$ . With this information, diffusion velocity  $V_d$  (parallel to the field line) was derived using the equation given in *Salah and Holt* [1974] where neutral densities and temperature were provided by the National Research Laboratory-Mass Spectrometer Incoherent Scatter (NRL-MSIS) model [*Picone et al.*, 2002]. With known  $V_{par}$  and  $V_d$ , geomagnetic meridional neutral winds  $U_n$  (poleward positive) were then calculated using the expression  $-U_n = (V_{par} - V_d)/\cos I$ .  $U_n$  was calculated only for  $F$  region heights above 200 km. The winds calculated for individual heights can sometimes show a clear height dependency. For this study, results given as Millstone Hill geomagnetic meridional winds  $U_n$  represent altitude averages within  $\pm 50$  km around the  $F_2$  peak height, weighted with error estimates of the individually derived values. The uncertainty on resulting neutral wind values was assigned as the maximum offset between this average wind around the  $F_2$  peak and the weighted average wind for 50 km above as well as below the  $F_2$  peak, and therefore represents the uncertainty associated with height dependency of the winds. Note that the traditional  $O^+ - O$  collision frequency value [*Dalgarno*, 1964] was used for the Millstone Hill wind calculations in the current study. A major uncertainty in the wind calculation arises for the use of an empirical neutral atmospheric model which affects  $V_d$  calculation primarily through the  $O^+$  and neutral collision frequency. However, the critically important plasma pressure gradient (in height) is determined directly by the ISR observations.

In summary, the regional and local measurements (with elevation  $\geq 45^\circ$ ) are used to determine the plasma drift vector and facilitate the calculation of thermospheric meridional winds. MHO meridional winds and their relationship with parallel plasma drift  $V_{par}$  are shown in Figure 8 and are discussed in detail in sections 3.3 and 3.7.

#### 2.2.4. Arecibo Observations

The Arecibo incoherent scatter radar conducted its 17 March 2015 campaign using both its Gregorian reflector and delay line feed to measure the ionospheric parameters using a coded long-pulse waveform [*Sulzer*, 1986]. A continuous beam swinging pattern, rotating over  $360^\circ$  in azimuth with  $75^\circ$  elevation and taking 16 min to complete a full cycle, measured  $los$  ion velocities to determine the three orthogonal components of the ion drift velocity vector. We subsequently used a least squares fitting approach within each  $los$  bin of 30 min in time and 100 km in height to resolve  $F$  region  $V_{perE}$ ,  $V_{perN}$ , and  $V_{par}$ .  $V_d$  is determined in a manner similar to Millstone Hill processing, except that height gradients are derived from the profiles after fitting with a polynomial of degree 3. Also, due to the high available accuracy of Arecibo measurements, we attempted to adjust the traditional  $O^+ - O$  collision frequency by applying the so-called Burnside factor ( $B_f$ ) [*Burnside et al.*, 1987] and found that  $B_f = 1.3$  (close to the *Pesnell et al.* [1993] result) resulted in better agreement between the ISR and FPI  $F$  region magnetic meridional winds than use of  $B_f = 1.0$ . Nevertheless, we stress that the use of different  $B_f$  values for MHO and AO should not be interpreted as location dependence of  $B_f$ , and furthermore, this procedure does not affect discussions associated with wind results.

#### 2.2.5. Other Observations

Additional observations involved in this study include global GPS total electron content (TEC) maps, Millstone Hill and Arecibo FPI neutral winds, and DMSP in situ plasma drift measurements. GPS TEC data are from MIT Haystack Observatory's GPS TEC analysis package [*Rideout and Coster*, 2006], upgraded recently with improved bias estimation [*Vierinen et al.*, 2016]. Millstone Hill FPI data used for this particular event are a subset of the data used in *Zhang et al.* [2015], and descriptions on them are provided in the paper and references therein. In particular, *Zhang et al.* [2015] indicated that significant vertical wind amplitudes did not seem to occur during the 9 h FPI observation on 18 March 2015 reported here. *Hairston et al.* [2016] provide a recent description of DMSP plasma drift observation characteristics.

All these data, along with the ISR data mentioned earlier, were obtained from the Madrigal database hosted by the MIT Haystack Observatory at <http://www.openmadrigal.org>.

### 3. Results and Discussion

Results and discussion are subsequently presented in the following topical order: (1) SAPS, strong ion convection, and SEDs in the Millstone Hill vicinity measured with the Millstone Hill ISR, DMSP, and the GPS TEC network; (2) penetration electric fields and potential disturbance dynamo effects during nearly the same interval

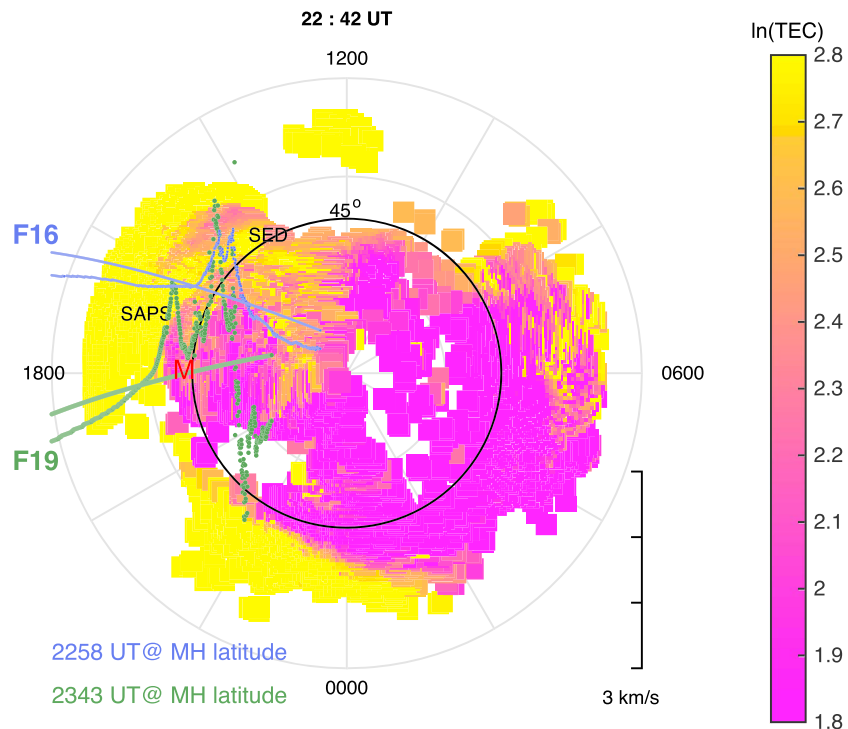


**Figure 3.** Northern polar view of total electron content at 22:42 UT on 17 March 2015, overlapped with DMSP F16 (gray) and F19 (magenta) cross-track ion velocities around 22:58 UT and 23:43 UT near Millstone Hill latitudes, in the  $\sim 16$  and  $\sim 18$  MLT planes. Geographic coordinates are used. The scale for the cross-track velocity is given at the bottom right of the dial plot.

when strong plasma flows or SAPS were measured by the MHO radar and DMSP; (3) Millstone Hill and Arecibo neutral winds; (4) Arecibo electric field oscillations; (5) Millstone Hill ionospheric  $F$  region heating associated with high-speed plasma flows; (6) corresponding  $E$  region ionospheric heating; (7) atmospheric upwelling (vertical winds); (8) ion outflow and frictional heating; and (9) ionospheric  $F_1$  region disturbances.

### 3.1. SAPS and SED Plume During 20–24 UT

During the storm,  $F_2$  peak electron density at middle and high latitudes over the American sector was lower than quiet conditions during sunlit hours [Zhang *et al.*, 2015; Astafyeva *et al.*, 2015; Liu *et al.*, 2016]. This was due to the influence of storm time  $O/N_2$  depletions that developed during the  $\sim 12$  h main phase period of the geomagnetic disturbance. At  $\sim 14$  UT when Thermosphere, Ionosphere, Mesosphere Energetics and Dynamics/Global Ultraviolet Imager was above Millstone Hill, significant  $O/N_2$  depletion was observed [Astafyeva *et al.*, 2015].

A few hours later, SED plumes were observed in Millstone Hill's longitude sector [Zhang *et al.*, 2015; Liu *et al.*, 2016], and around  $\sim 20$  UT the plume passed over Millstone Hill. Figure 3 shows a northern polar view of TEC at 22:42 UT where a clear plume can be seen slightly southward of Millstone Hill (marked as the letter "M") extending westward and northward. We note that SED plume passage right above Millstone Hill was observed slightly earlier at  $\sim 20$  UT [Zhang *et al.*, 2015].

Overlaid on Figure 3 are DMSP F16 and F19 cross-track ion velocities which are most sensitive to east-west drifts along their dusk sector orbital paths. F19 was close to magnetic local time (MLT) dusk and showed two strong westward flow peaks, with (1) SAPS identified as the flow peak on the equatorward side near the zone of sharply reduced TEC from the SED plume poleward and (2) strong ion convection identified as the other poleward peak. Farther to the north, reversed convection in the polar cap was observed. F16's orbit observed conditions approximately 1 h before dusk and exhibited very similar SAPS and convection structures. Note that spatial separation between SAPS and auroral convection for F16 is smaller than for F19, and the SAPS location in F19 is at a lower latitude than that in F16. This MLT dependence of SAPS location (latitude) agrees roughly with statistically derived results from Foster and Vo [2002] and Erickson *et al.* [2011].



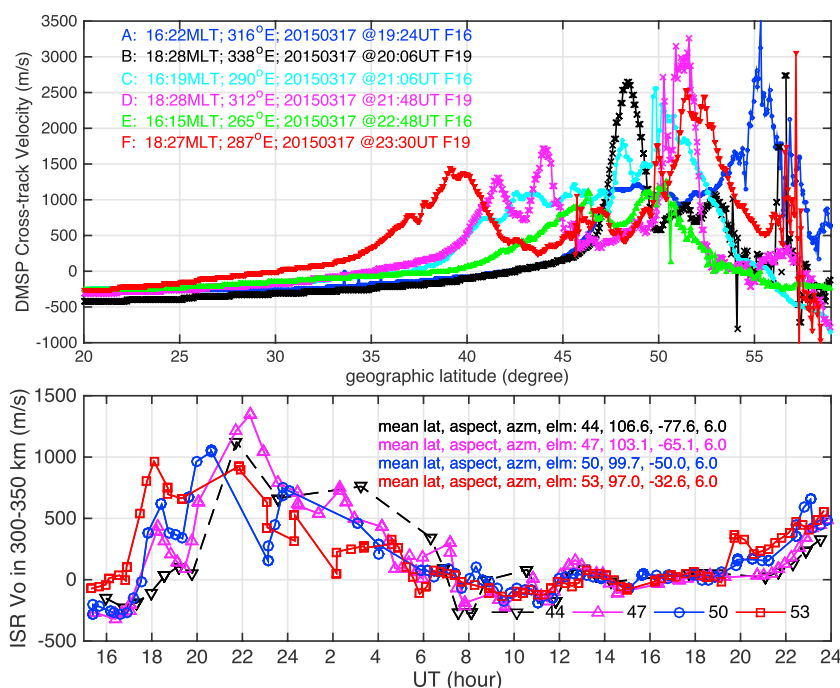


**Figure 4.** Spatial-temporal features of SAPS and large plasma drifts measured by (top) DMSP F16 and F19 satellites and by Millstone Hill (bottom) ISR. Cross-track ion velocity from three F16 and three F19 crosses over the American sector were selected; MLT, UT, and longitude for the geographic equator which the satellite crossed are marked. SAPS are found at latitudes ranging from 50°N down to 40°. Millstone Hill ISR observations of plasma drifts are shown as line-of-sight velocity ( $V_o$ ) at four latitudes to the north of the radar, which are averaged over 300–350 km. Strong plasma flows occur between 20 and 24 UT 17 March and indicate the presence of SAPS as well as enhanced convection.

Figure 3 also depicts the spatial relationship between the SAPS and SED plume. As expected from earlier studies [Foster *et al.*, 2007], SAPS and SED are not coaligned in space, with SAPS located near the poleward edge of the plume.

Two additional passes of DMSP F16 and F19, respectively, over the North American sector between 19 and 22 UT (immediately before those shown in Figure 3) also show clear signatures of SAPS or large plasma drifts near MHO latitudes or slightly northward (Figure 4 top). These large drifts were  $\geq \sim 1000$  m/s in amplitude. Again, DMSP F16 passes with an earlier MLT had this SAPS or large plasma drift feature at higher latitudes than the F19 ones with a later MLT. Therefore, it is quite reasonable to assume the existence of SAPS or large ionospheric drifts in the MHO vicinity during the 20–24 UT time frame.

The temporal correlation between the appearance of both SAPS and the SED plume is further demonstrated in MHO observations, as ground-based ISR experiments provide superior temporal resolution for temporal variations of plasma flows (SAPS and convection). In particular, signatures of SAPS and convection can be seen in the *los* ion drifts measured with the Millstone Hill radar's low elevation scans, as shown in Figure 4 (bottom). When looking to the west with azimuth between  $-50$  and  $-80^\circ$ , a significant westward ion drift component contributed to the *los* velocity in the *F* region since the aspect angle (the angle between the radar beam and magnetic field) is  $\sim 100^\circ$ . The ion velocity experienced a sharp increase after 18 UT reaching maxima at  $\sim 22$  UT in a broad latitude range from 44 to 53°N [Yeh *et al.*, 1991], but the highest speeds were between 44 and 47°N (within 5° to the north of Millstone Hill), and the speeds were lower at higher latitudes. Also, the time of the peak *los* occurred earlier at high latitudes than at lower latitudes. It is not immediately clear from this figure alone which of these features are SAPS, but in any case these were high-speed ion flows that could have contributed to SED plume development and furthermore could have affected local heating and thermal balance as discussed later. It is clear that observations during the time frame from 20 to 24 UT when *los* was significantly enhanced are consistent with the existence of SAPS and large plasma drifts near MHO observed with DMSP satellites as shown in Figure 4 (top).

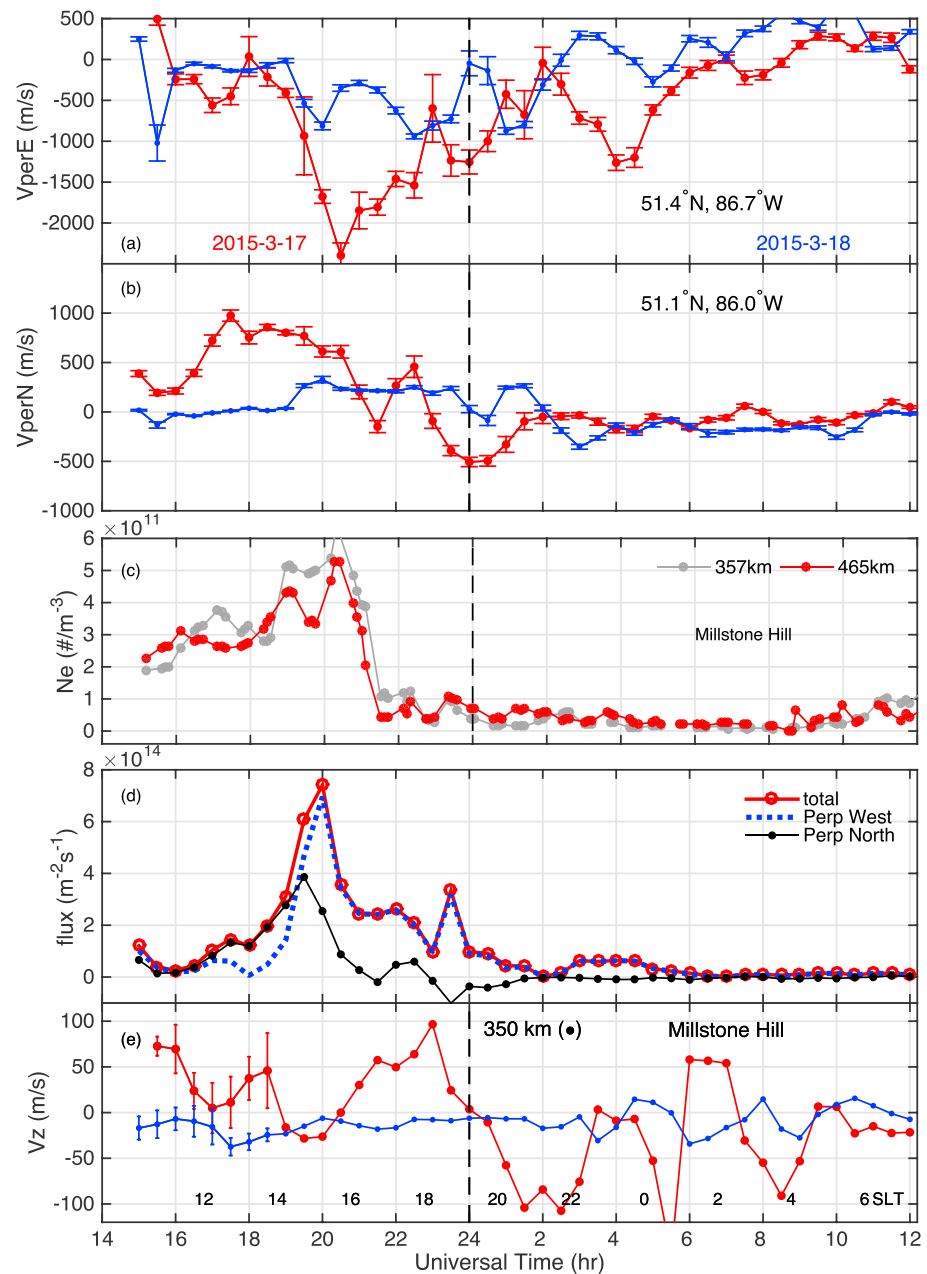


**Figure 5.** (a and b) Convection speed estimated to the north of Millstone Hill using the radar's wide coverage experiment between 300 and 450 km, as well as vertical ion drifts ( $350 \pm 10$  km) local to (e) Millstone Hill. Red curves begin on 17 March, and blue ones begin on 18 March. (c) Electron density as a 15 min median within  $\pm 18$  km around 357 km (gray dots) and 465 km (red dots). (d) Total cross-field flux (red solid), the flux in magnetic zonal direction (blue dotted), and flux in magnetic meridian direction (black solid), all within 300–350 km at  $\sim 50^\circ\text{N}$  (corresponding to the blue line in Figure 4, bottom).

By combining *los* velocity data from MHO low elevation scans, we determined convection velocities  $V_{perE}$  and  $V_{perN}$  (Figure 5).  $V_{perE}$  became very strongly westward reaching  $>2000$  m/s at  $51.4^\circ\text{N}$  between 20 and 24 UT (near or prior to dusk, Figure 5a). Zhang *et al.* [2015] showed similarly enhanced westward flow at  $47^\circ\text{N}$  but with a smaller magnitude ( $<1000$  m/s). These results are comparable with the DMSP cross-track velocity shown in Figures 3 and 4. While  $V_{perE}$  was relatively weak on the dayside (prior to 20 UT), enhanced dayside northward (upward) flow in  $V_{perN}$  (prior to 20 UT) was evident (Figure 5b).

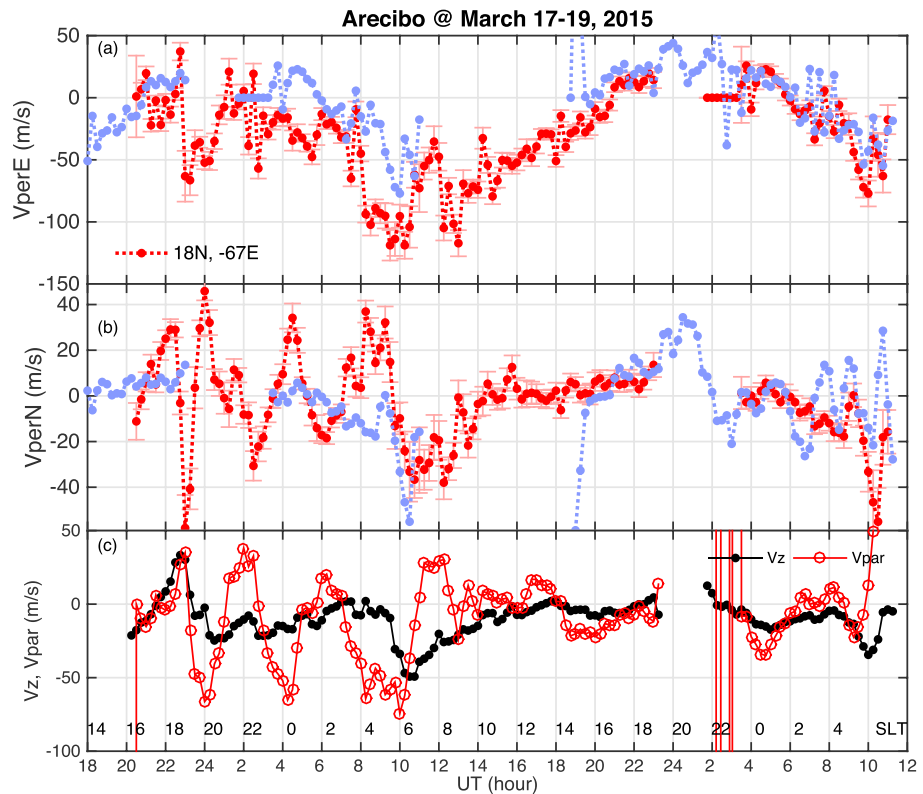


**Figure 6.** Similar to Figure 4 but for Arecibo: (a)  $V_{\text{perE}}$ , (b)  $V_{\text{perN}}$ , and (c)  $V_z$  and  $V_{\text{par}}$  at 350 km. Red (and black) curves show data starting on 17 March, and blue curves show data starting on 18 March.

The passage of a SED plume over Millstone Hill at  $\sim 20$  UT (local afternoon) appeared in electron density enhancements (Figure 5c) and ionospheric  $F$  region electron content [Zhang *et al.*, 2015] immediately prior to or at the onset of local large plasma drifts which existed between 20 and 24 UT (before or around dusk). This indicates that westward transportation carried plasma from later MLT times toward the east across Millstone Hill, i.e., from dusk/evening to afternoon MLT sectors. Along with these strong westward flows at late MLT period (close to dusk), poleward transportation occurred at earlier MLT close to noon to the northwest of MHO. The vertical component of the transport moved plasma from low altitudes associated with large photoionization production to high altitudes where chemical recombination was significantly slower. The net effect of transportation in these directions was evident in accumulation of plasma to form the SED plume, and this scenario was confirmed for this event by a separate numerical study [Liu *et al.*, 2016]. Figure 5d shows the cross-field plasma flux within 300–350 km at  $\sim 50^\circ\text{N}$  (corresponding to the blue line in Figure 4, bottom). The flux intensified to a maximum value of  $8 \times 10^{14} \text{ m}^{-2}\text{s}^{-1}$  at 20 UT when the westward drift maximized. At this time, contributions from magnetic meridional transport were significant as well, reaching a maximum slightly earlier than the magnetic zonal transport contribution. The same northward/upward drift could have also transported plasma from subauroral latitudes into the cusp region where it would subsequently enter the polar cap as part of the tongue of ionization [Foster *et al.*, 2005]. These observations of TEC as well as ion drifts from the ISR and DMSP from this great storm are consistent with existing understanding of the roles of strong westward convection and large northward/upward drift in forming and evolving SED features [Foster, 1993; Heelis, 2008; Yuan *et al.*, 2009; Zou *et al.*, 2014, and references therein].

### 3.2. Prompt Penetration Electric Field Versus Disturbance Dynamo

During the storm event from 14 to 24 UT, the interplanetary electric field (IEF) was strong at the level of  $\sim 10 \text{ mV/m}$ . IEF fluctuated with peaks near  $\sim 16$ – $18$  UT and  $\sim 22$  UT. Both MHO ISR and DMSP observations (Figure 7, to be discussed later) near these two time periods contain enhanced poleward perpendicular ion drifts/vertical upward drifts (due to eastward electric field) and signatures of penetration electric field: the  $V_{\text{perN}}$  enhancement prior to 21 UT to the north of MHO (Figure 5b) and the weak  $V_{\text{perN}}$  enhancement locally at MHO near 18 UT (Figure 8b).

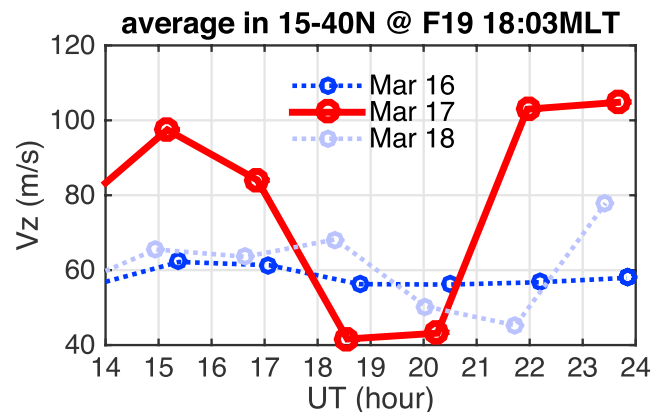


**Figure 7.** DMSP F16 measurements of vertical ion drift  $V_z$ , averaged over middle and low latitudes ( $15\text{--}40^\circ\text{N}$ ) around the dusk sector for 16–18 March 2015. Enhanced vertical drifts appear on 17 March, associated with large IEF  $E_y$  ( $>10$  mV/m) between 14–16 UT and 21–24 UT in Figure 1.

$V_{\text{perN}}$  showed an isolated increase at  $\sim 22$  UT at dusk, when the plasma flow is mostly poleward/sunward (Figure 5b). This  $V_{\text{perN}}$  enhancement was observed to the north of MHO, coincident with enhancement in local MHO vertical drift  $V_z$  (Figure 5d). Note that this  $V_z$  enhancement at 22 UT was different from the earlier signature at 18 UT that contributed to SED plume development. In particular, the 22 UT excursion did not cause significant Ne increase since the ionosphere to the west of MHO was unable to supply sufficient ionization to the enhanced westward convection. This west side ionosphere had been involved in transporting ionization to the earlier (20 UT) SED plume and, in addition, was experiencing low photoionization toward sunset. Therefore, local Ne at 22 UT did not increase, and this was followed by the plasmaspheric boundary sweeping over Millstone Hill prior to the arrival of the midlatitude main trough and a rapid decrease in background Ne.

At lower latitudes (Figure 6), the northward electric field (zonal ion drift) was also visible at Arecibo, with a sudden westward drift enhancement in  $V_{\text{perE}}$  between 22 and 01 UT on 17–18 March. The eastward electric field (meridional ion drift  $V_{\text{perN}}$ ) fluctuated in the dusk and evening sectors with amplitudes well beyond quiet time values. Around the same time of  $V_{\text{perE}}$  westward sudden increase,  $V_{\text{perN}}$  was suddenly southward, indicating an externally imposed westward electric field. Figure 6 also indicates that the  $V_z$  variation prior to 23 UT variation follows closely the behavior of  $V_{\text{par}}$  (i.e., neutral winds and diffusion velocity) but not that of  $V_{\text{perN}}$  (zonal electric field). It should be noted that at this stage of the storm ( $\sim 22$  UT or 18 LT at AO), the traveling atmospheric disturbance (TAD) and the disturbance neutral wind were about to reach or even might have reached AO (section 3.3). This TAD could have potentially generated a disturbance dynamo [e.g., *Blanc and Richmond, 1980*], contributing to the enhanced westward  $V_{\text{perE}}$  and southward  $V_{\text{perN}}$ . On the other hand, evidence for penetration electric field effects during this same period, in addition to the MHO results, also exists.

A comprehensive survey of DMSP drift data during this 17 March 2015 storm showed that the penetration electric field reached down to  $20^\circ$  magnetic latitude on the duskside [*Hairston et al., 2016*]. DMSP F16 and F19 observations of vertical plasma drift showed a clear enhancement before 18 UT and after 21 UT; Figure 7 demonstrates this using the F19 averaged vertical drift  $V_z$  at middle and low latitudes between  $15$  and  $40^\circ\text{N}$  at locations where the ISR data showed externally imposed electric field signatures.

To summarize, all these observations suggest that the prompt penetration electric fields over MHO vicinity can be clearly identified during two duskside segments, 17–20 UT and 22 UT, but at AO the disturbance dynamo electric field appears to come into play around 22 UT along with the penetration electric field.

### 3.3. Meridional Neutral Winds and Traveling Atmospheric Disturbance

During main storm phase, meridional neutral winds near the  $F_2$  peak height showed dramatic changes, with strong latitudinal variations causing very different signatures over Millstone Hill (Figure 8a) and Arecibo (Figure 9).

At Millstone Hill's subauroral location, storm time neutral winds showed the following features:

1. A significant equatorward neutral wind surge on the dayside peaking at  $\sim 200$  m/s at 16 UT, much stronger than that on a quiet day. In the nightside Asian sector, nearly simultaneous equatorward wind surges were

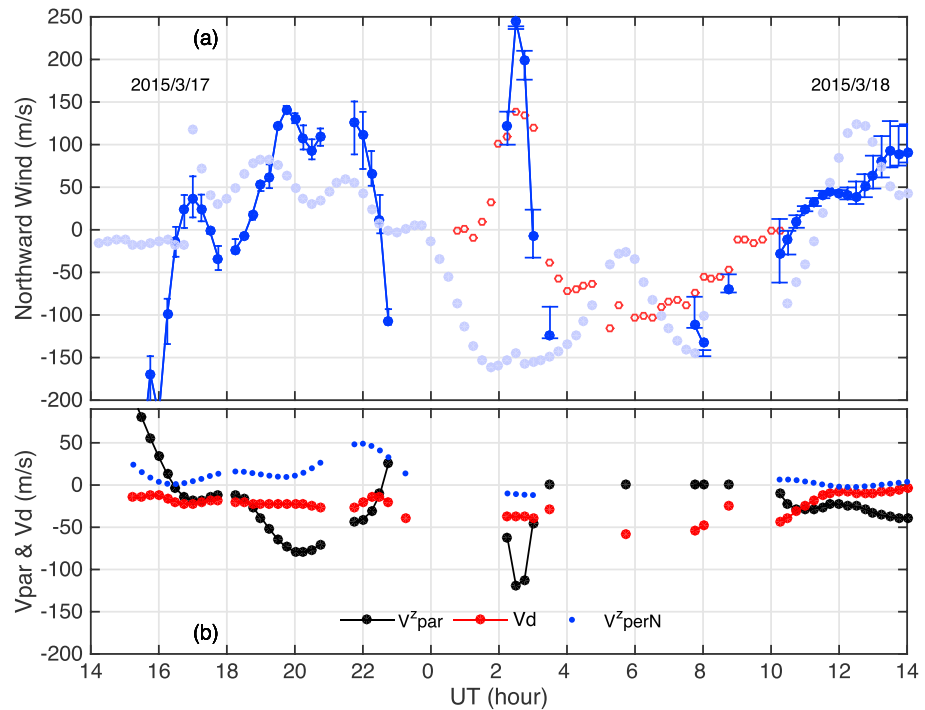


**Figure 8.** (a) Geomagnetic meridional winds at Millstone Hill, measured near the  $F_2$  peak height by the ISR (blue) and by the on-site FPI (red). The blue error bars indicate the range of the wind magnitude within 20 km around the peak value. The light blue curve plots the same winds but for 20–21 March with quiet magnetic activity. (b) The diffusion velocity  $V_d$ , the field-aligned ion velocity  $V_{par}$  projected vertically  $V_{par}^z$ , and perpendicular northward velocity  $V_{perN}$  projected vertically  $V_{perN}^z$  are also shown as averages within 250–300.

also observed at Shigaraki (34.9°N, 134.8°E) in the Northern Hemisphere and Darwin (12.4°S, 131.0°E) in the Southern Hemisphere [Tulasi Ram *et al.*, 2016]. The quiet time meridional wind on the dayside is typically poleward as part of the general thermospheric circulation. However, during the 17 March 2015 storm, the large equatorward surge was superimposed on this background poleward wind and lasted for a short time. A storm time dayside equatorward wind surge is not observed as often as a nightside surge, but Goncharenko *et al.* [2007] provided such an equatorward wind surge example during a moderate storm. Simulations by Lu *et al.* [2008] indicate that Joule heating confined to the dayside convection zone is a sufficient driver for production of an equatorward wind enhancement and can be responsible for a positive phase storm.

- Quasiperiodic oscillations with a 2–3 h period between 16 and 23 UT, that have an apparent association with large-scale traveling atmospheric disturbances (TAD, see, for example, Shiokawa *et al.* [2002, 2003] for observations at middle and lower latitudes). The storm time TAD is much larger in amplitude than quiet time wave-like oscillations. The quasiperiodic oscillations are superimposed on the storm time dayside surge mentioned above and also on the regular quiet time wind circulation pattern. The surge and large amplitude TAD are bright and characteristic responses to storm driven high-latitude heating, but it is unusual to observe both signatures nearly simultaneously, as the phase velocity for large-scale TAD propagation is not necessarily the same as the propagation velocity of the surge. (The latter is established by an enhanced equatorward pressure gradient force of the neutral atmosphere superimposed on the regular general circulation.)
- Within approximately 1 h starting from 22 UT, the derived meridional wind reduced significantly its northward component and turned equatorward. The 250 m/s wind speed change in an hour, from 150 m/s northward to 100 m/s southward, was not part of the regular quiet time wind circulation near sunset which causes a rotation in wind direction and a typical speed change of 150 m/s in an hour after 24 UT. It was also not part of the neutral wind oscillation mentioned above, because the ionospheric density did not oscillate similarly with any signature of the propagation phase change in height during 20–22 UT (see Figure 10). These effects can be explained in terms of either a southward wind impulse which could be generated

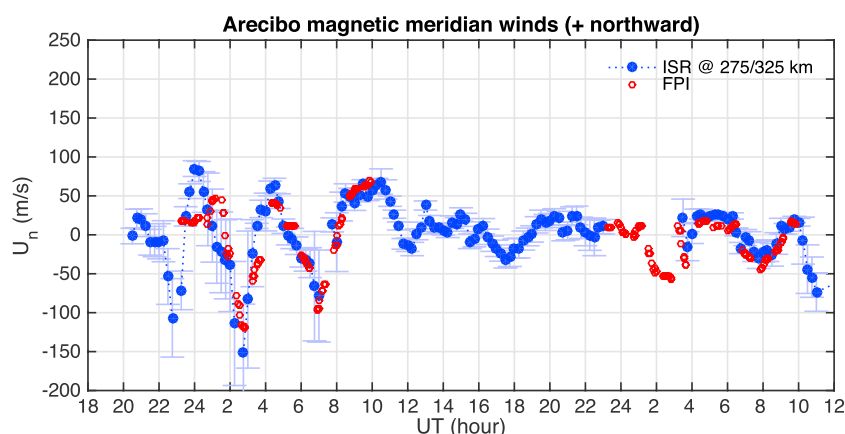


**Figure 9.** Same as Figure 7 but for the Arecibo site. The wind calculation here used a 1.3 Burnside factor for the  $O^+ - O$  collision frequency correction.

remotely at higher latitudes or a vertical wind that occurred locally. In particular, this rapid meridional wind variation could be an indicator of local neutral atmosphere upwelling following strong frictional heating associated with strong plasma flow (as shown in Figures 4 and 5a). In a normal ISR neutral wind calculation procedure, vertical winds are not taken into consideration, and so situations contaminated with a strong upward wind will produce an apparent southward wind analysis artifact. The frictional heating arguments will be presented later. These derived meridional winds correspond to an enhancement (by 50 m/s) of the upward ion drift (Figure 5d), which then became downward reaching a maximum speed in 4 h. Nevertheless, inherent ambiguity exists because a southward wind impulse and a vertical upwelling wind can impose a similar rapid southward turning signature (or a significantly reduced northward component). The gap of the derived winds was due to interference (coherent plasma irregularity occurrence that masked normal incoherent scatter returns) within the MISA measurements at 45° elevation.

4. Poleward wind surge near 02 UT on 18 March, as seen by both ISR and FPI (red circles in Figure 8a). Zhang *et al.* [2015] indicated that this premidnight surge, as opposed to the well-known midnight equatorial surge, is a result of westward neutral winds driven by SAPS high-speed ion flows in the same westward direction via ion-neutral collisions. The strong westward neutral wind can also induce a northward wind through the Coriolis force. Similar poleward wind surges and related westward enhancements were also found at approximately the same time over sites to the west and slightly south of Millstone Hill. Additional arguments from this present study show that both the ISR and FPI had similar poleward wind surges at approximately the same time. We note as well that impulse-like poleward wind surges cannot be ascribed to TAD, since they exhibit non-wave-like characteristics such as a huge amplitude offset from a quiet time wind (by well above 300 m/s) and a quick decay of poleward wind without any further oscillation.

At low middle latitudes, Arecibo neutral winds showed quite different responses to the storm (Figure 9). While Arecibo winds were slightly more equatorward on average on 17–18 March between 20 and 08 UT (dusk and nighttime sectors) compared to the next day, the storm time large wind amplitude (100–200 m/s) and long period ( $\sim 4$  h) oscillation is a striking feature. This is the case for the magnetic meridional winds derived from both ISR (blue) and FPI (red) data sets. The oscillation is part of the wave-like TAD which is also seen in the winds at Millstone Hill mentioned earlier.

It was not feasible to determine a timing relationship between the waves seen at Millstone Hill and Arecibo due to lack of data prior to 20 UT at Arecibo. However, regional TEC maps over the continental U.S. (not shown) clearly indicate the progression of a large-scale traveling ionospheric disturbance (LSTID), the ionospheric manifestation of a TAD. The LSTID structure associated with TAD passage can be also found in the two-dimensional electron density contours (UT and altitude) locally at MHO and AO (Figure 10). These TID signatures in radar measured electron density have classical gravity wave-related features [Kirchengast *et al.*, 1996]. In particular, Ne disturbances at MHO clearly show 2.5 h wave structures primarily in the  $F_2$  region, progressing with a large delayed phase toward lower altitudes. At AO where radar topside ionospheric measurements are available, electron density oscillation valleys and peaks show evidence of delayed phase toward lower altitudes between 0100 and 0400 UT on 18 March.



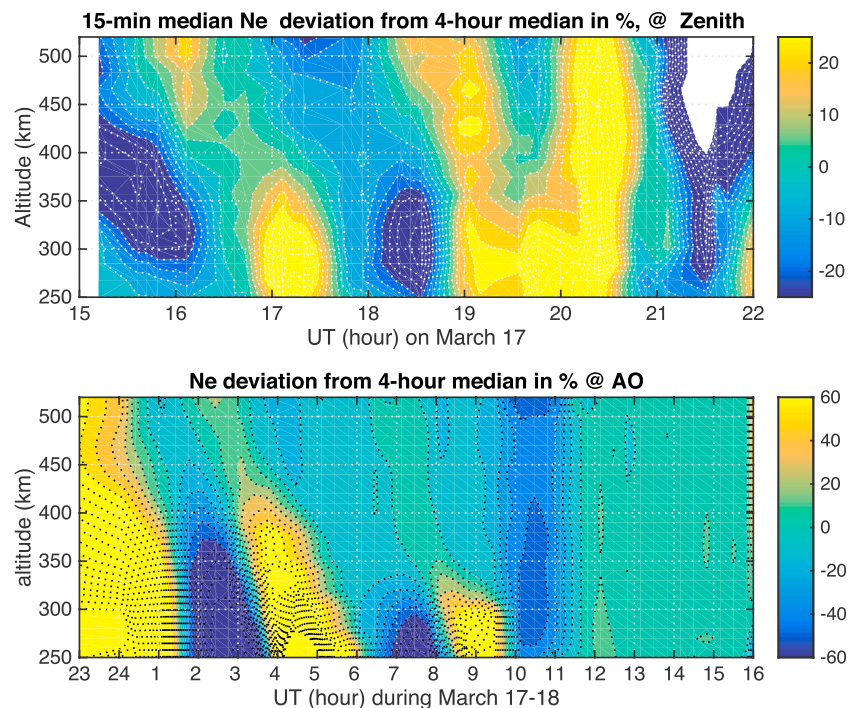


**Figure 10.** *F* region electron density height versus universal time variations at (top) MHO and (bottom) AO, shown as the percentage deviation from the 4 h median of electron density in  $\text{m}^{-3}$ . An enhancement immediately after 20 UT at MHO indicating the local passage of storm enhanced density (SED).

### 3.4. Oscillations of Electric Fields

The wave-like TAD signature was very prominent in oscillating meridional winds observed at Arecibo. A very similar electric field oscillation was present at Arecibo as well (Figure 6).  $V_{\text{perN}}$  had peaks and valleys in dusk, evening, and nighttime hours from 23 UT onward (recall that the peak before these times was ascribed earlier to the penetration electric field). These  $V_{\text{perN}}$  oscillations (Figure 6b) were negatively correlated with the parallel ion drift  $V_{\text{par}}$  (Figure 6c). The oscillating  $V_{\text{par}}$  was mainly driven by the meridional winds (Figure 9), as horizontal wind changes caused corresponding ion parallel motions, and therefore, we associate the meridional wind oscillation with the electric field oscillation.

Significant anticorrelation between  $V_{\text{par}}$  and  $V_{\text{perN}}$  creates mostly horizontal bulk plasma motion [Buonsanto and Foster, 1993]. This feature has been extensively observed by Arecibo and Millstone Hill ISRs [Behnke and Harper, 1973; Buonsanto and Foster, 1993], but the detailed mechanism remains an unresolved puzzle in spite of many attempts [Rishbeth et al., 1978; Walker, 1980]. One suggested mechanism is associated with the polarization electric field established by the *F* region neutral wind dynamo, an important feature as responses of the electric fields to meridional wind changes occur nearly instantaneously owing to the vast difference between ionized and neutral density. This polarization field mechanism works only if the flow of *F* region current is inhibited by ionospheric horizontal (zonal) variations. We argue in the storm studied here that the upper atmospheric conditions which developed are capable of satisfying the required (1) neutral wind disturbances and (2) ionospheric zonal inhomogeneity. The TAD in meridional winds were likely associated with propagating gravity waves launched by geomagnetic activity, as evidenced at Millstone Hill and Arecibo. These perturbations therefore drove variations in the *F* region Pederson (zonal) current flow. The current flow experiences ionospheric density gradients in the zonal direction, as it was initially located close to the dusk terminator. Another factor in this event's polarization electric field development was significant spatial gradients in the wave-like ionospheric density due to zonal gradients in the ionospheric conductivity. For these reasons, we assert that observed anticorrelation between  $V_{\text{par}}$  and  $V_{\text{perN}}$  ultimately reflects the existence of a polarization electric field perturbation generated by the large-scale TAD. (Similar polarization electric fields for the time period with medium-scale TID (MSTID) perturbations also exist in nighttime sectors) [Saito et al., 1995; Otsuka et al., 2004; Huang, 2016.]

### 3.5. *F* Region Heating

During the SAPS (large ionospheric drift) time period at 20–24 UT, the ionosphere and thermosphere underwent substantial variations. These variations started around 21 UT and had the following characteristics:

1. Vertical drift  $V_z$  enhanced from 50 m/s to 100 m/s upward between 2200 and 2330 UT (Figure 11, top). Figure 4 shows the penetration electric field around this time at 10° north of MHO. This electric field also occurred locally at MHO (Figure 8b). The vertical drift  $V_{\text{perN}}^z$  driving by the penetration could account for most of the 50 m/s  $V_z$  prior to the 100 m/s peak  $V_z$  at 23 UT, but not the peak  $V_z$ . On the other hand, as shown in Figure 8b, the vertical drift  $V_{\text{par}}^z$  arising from the parallel drift was subject to rapid change by  $\sim 70$  m/s in an hour between 22 and 23 UT, turning from downward to upward. Therefore, the parallel drift contributed the most to the large  $V_z$  enhancement. During the rapid  $V_{\text{par}}^z$  change, the change in diffusion velocity  $V_d$  was modest. Therefore, it seems logical to ascribe this parallel drift and vertical drift feature to the equatorward meridional wind. However, we further argue that mainly because of the accompanying large  $T_i$  enhancement (discussed immediately below), the observed  $V_z$  and  $V_{\text{par}}$  enhancements (22–23 UT) could be also related to ion upwelling driven by neutral upwelling (or vertical winds). The upwelling signature in radar derived neutral winds was previously mentioned in section 3.3, and the next section (3.6) will address the *E* region upwelling.
2. Enhanced ion temperature  $T_i$  by up to 700 K in the  $F_2$  region (Figure 11, middle). The ion temperature change  $\Delta T_i$  due to frictional heating is proportional to the squared ion-neutral relative velocity  $\delta V_{i-n}^2$  [Schunk and Nagy, 2000]. In the  $O^+$  dominant *F* region, this  $\Delta T_i$  of 700 K means that the relative speed  $\delta V_{i-n}$  was 1000 m/s. Both ion and neutral velocities in the meridional direction are very small (see Figures 3 and 5; note that these are not exactly over Millstone Hill. See also Figure 8), and the ion-neutral relative velocity in this direction should be small. However, the zonal ion drift was much larger than the meridional ion drift (Figures 3 and 5), and the relative ion-neutral velocity could have been much larger in zonal direction than in meridional direction. However, without measurements of the zonal neutral wind, it is impossible to obtain the exact ion-neutral relative velocity. The zonal wind is known to respond strongly to SAPS forcing [H. Wang et al., 2011; Wang et al., 2012; Zhang et al., 2015]. It is reasonable to speculate that the relative velocity could have been as large as 1000 m/s.
3. Elevated  $T_i$  values similar to those observed should enhance the chemical reaction rates between  $O^+$  and  $O_2$  or  $O^+$  and  $N_2$ , potentially leading to an *F* region  $O^+$  density reduction. The *F* region density reduction occurred immediately after the SED plume passage over Millstone Hill (Figure 10). The passage was during a period characterized by (1) lack of sufficient plasma source produced by photoionization on the dusk-side/nightside that can be transported to the MHO vicinity, (2) arrival of the midlatitude trough, and (3) influences of the neutral composition caused negative storm phase. We also point out that enhanced chemical loss due to the elevated  $T_i$  was an additional factor contributing to the immediate  $F_2$  region density reduction.

Simulation of SAPS-driven thermospheric responses has been previously performed by Wang et al. [2012]. Based on the results, expected ionosphere and thermosphere signatures during SAPS forcing periods include enhancements in zonal winds and the neutral temperature, and the *F* region ion temperature changes observed during 17–18 March 2015 fall within these expectations qualitatively. The observed effects for this particular event were generally much more strong. However, it should be noted that the measured  $T_i$  enhancement, large upward ion drift, and all the DMSP and ISR measured SAPS and larger ionospheric convection velocity (therefore the potential frictional heating) did not always coexist perfectly in space and time due to the spatial-temporal resolution constraints for this event's observations. The connection between frictional heating in the *F* region (and in the *E* region as well, to be discussed in the next section) and SAPS (or large ionospheric drift) must therefore remain largely speculative.

The following sections present observational evidence that a much wider range of upper atmospheric changes are possible due to strong electrodynamic perturbation causing storm time ionosphere, thermosphere, and magnetosphere response.

### 3.6. *E* Region Heating

We performed a storm perturbation analysis for Millstone Hill ISR data in the *E* region (100–130 km), and the results are shown in Figure 12. Ions in the *E* region plasma are by definition nearly unmagnetized due to collisions with very large neutral densities. However, Figure 12 indicates that the Millstone Hill observed *E* region storm time vertical ion drift reached  $\sim 100$  m/s (red curve) during the SAPS period between 21 and

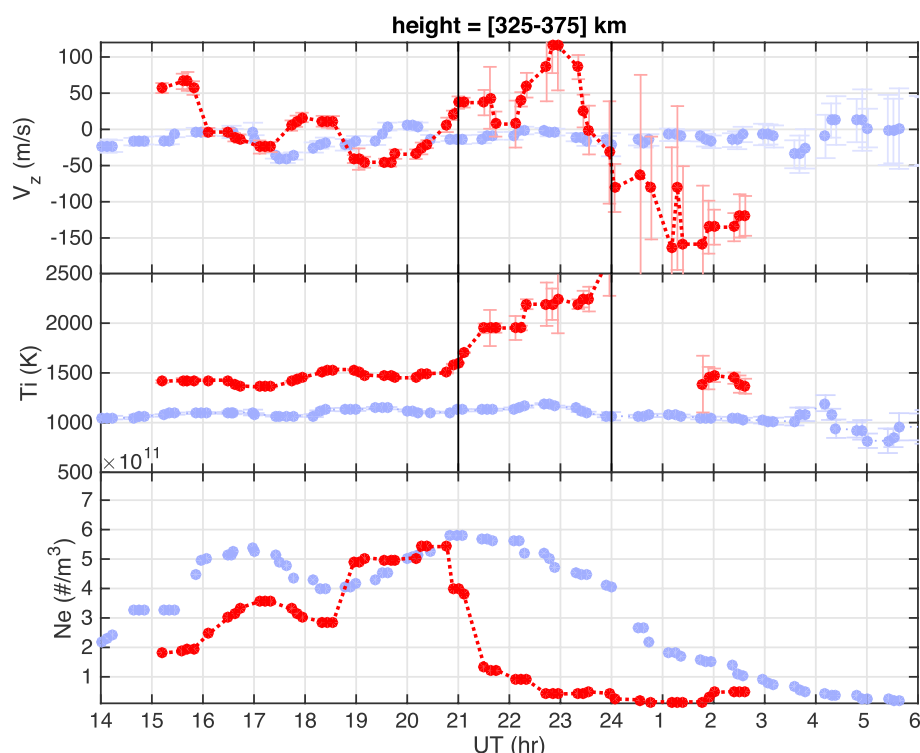


**Figure 11.** Millstone Hill *F* region storm time response signatures in (top) vertical ion drift, (middle) ion temperature, (bottom) and electron density averaged within 325–375 km, showing large plasma flow during the SAPS period (between black lines). The red symbols are data starting 17 March, and the light blue ones show 18 March data, a period of relatively weak magnetic activity.

24 UT, clearly above quiet day levels (blue curve). Prior to SAPS influence, *F* region  $V_{\text{perN}}$  (or equivalently the penetration electric field) to the north of MHO was 500–1000 m/s between 17 and 21 UT (Figure 5) and  $V_z$  at 105–125 km above MHO was close to zero during the same time (Figure 12). ( $V_{\text{perN}}$  at 105–125 km over MHO was not measured by the experiment pointing configuration.) One speculation is that the large MHO  $V_z$  observed during the SAPS period was not associated with the penetration electric field induced  $V_{\text{perN}}$  in the *E* region, as the zonal penetration electric field would need to be excessively large to yield a significant  $V_{\text{perN}}$  component in the *E* region. Rather, we ascribe storm time ion upwelling indicated by the large  $V_z$  to a variation imposed by upwelling neutrals. In this scenario, the vertical neutral wind perturbation, associated with neutral upwelling, was caused by ion frictional heating as a result of large ion-neutral relative velocity in the horizontal direction. This conjecture is supported by the observed ion zonal flow  $V_{\text{perE}}$  that was clearly much larger than  $V_{\text{perN}}$  (Figure 5).

*E* region frictional heating was also observed as a  $T_i$  enhancement during 21–24 UT (Figure 12, middle). At *E* region altitudes, an observed 200 K  $\Delta T_i$  corresponds to  $\delta V_{i-n} = 400$  m/s. This relative velocity is much smaller than the 1000 m/s ion-neutral relative velocity mentioned earlier, because of the much denser neutral atmosphere in the *E* region. The elevated  $T_i$  did not seem to cause significant reduction in *E* region electron density during its large diurnal variation toward sunset.

Figure 13 shows estimates of the integrated Pedersen and Hall conductivity over Millstone Hill for the entire study period in both the *E* region (100–150 km) and *F* region (200–550 km), as well as total conductivity over the 100–550 km range. The conductivity calculation, based on the Schunk and Nagy [2000] formulation, was performed using ISR plasma density and temperatures along with NRL-MSIS modeled neutral parameters [Picone et al., 2002]. Even though large changes in both conductance parameters occurred in the *F* region before and after SED plume passage, integrated conductance parameters were nearly completely dominated as expected by *E* region conditions. Since SAPS-related effects do not greatly influence *E* region electron density conditions, conductance variations were therefore not strongly correlated to SAPS related frictional heating. (We note that the *E* region conductance estimates have large postsunset uncertainty due to the

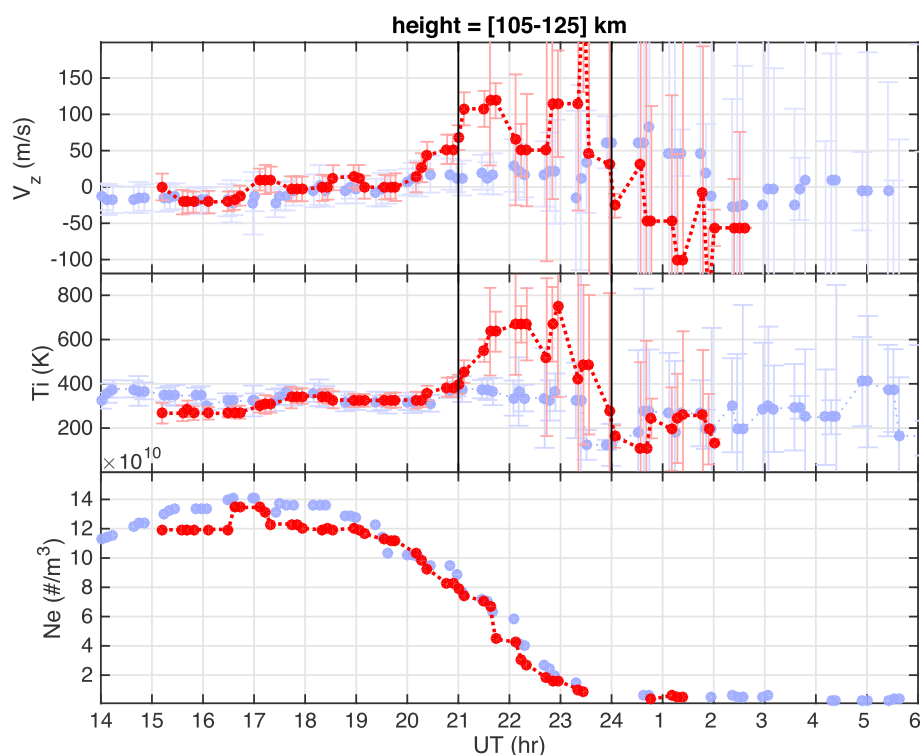


**Figure 12.** Millstone Hill *E* region storm time response signatures in (top) vertical ion drift, (middle) ion temperature, and (bottom) electron density averaged over 105–125 km, with the SAPS period marked by black lines. The red symbols are for 17 March data, and the light blue ones show 18 March data, a period of relatively weak magnetic activity.

low signal-to-noise ratio caused by low electron density values.) These results also indicate that strong SAPS can exist in the presence of a large conductivity *E* region. Under steady ion drift conditions, the total frictional heating to ions and neutrals is equal to Joule heating, and therefore, Joule heating can be also very large during the SAPS period (The large *E* region conductivity does favor this.) However, as the ion drift fluctuates, the Joule heating rate underestimates the total energy involved in the frictional heating [Brekke and Kamide, 1996].

### 3.7. Atmospheric Upwelling

Figure 14 summarizes Millstone Hill subauroral vertical ion drift  $V_z$  throughout the *E* and *F* regions during the storm event by plotting the  $V_z$  altitude profile averaged over an hour (22–23 UT) during the large  $T_i$  enhancement period, using MHO long-pulse waveform data for the *F* region and alternating code waveform data for the *E* and  $F_1$  regions. In the *F* region,  $V_z$  is 50–70 m/s faster (upward) than for a relatively quiet day and increases slightly over the duration of the storm event. In the *E* and  $F_1$  regions below ~200 km altitude, there is a similar vertical velocity enhancement of ~50 m/s during the SAPS period compared to quiet conditions. Large height gradients in vertical velocity exist near 150 km altitude for both quiet and disturbed conditions, but this seems a regular feature shown in meridional wind height profiles from climatology models such as Drob *et al.* [2008] and Emmert *et al.* [2008]. The largest *E* region storm time vertical drift enhancement is ~100 m/s between 120 and 150 km altitude. The more or less uniform nature of drift enhancements throughout the *E* and *F* regions strongly disfavors a predominant penetration electric field influence, which should fall dramatically in amplitude at low altitudes due to a dramatic increase in the ion-neutral collision frequency. It should be noted also that unless the neutrals move vertically in the *E* region, a substantial vertical velocity of the ions cannot last for 1 h in the *E* region.

We argue that the common driver for the subauroral vertical drift enhancement seen throughout the *E* and *F* regions was the atmospheric upwelling caused by strong ion-neutral frictional heating to both neutrals and ions during the SAPS period. Frictional heating and upwelling were established on a timescale of approximately an hour following the onset of strong horizontal ion flow relative to the neutrals, and these effects subsequently enhanced the vertical ion drift throughout the *E* and *F* regions.

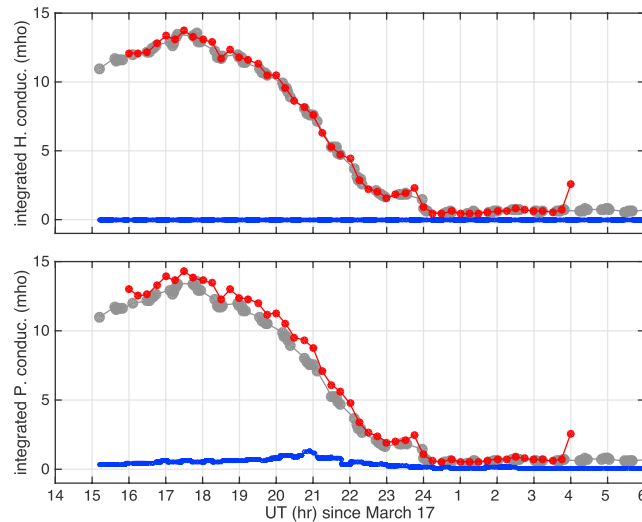


**Figure 13.** Estimated (bottom) Pedersen and (top) Hall  $E$  region integrated conductance for the  $E$  region (100–150 km, gray dots), the  $F$  region (200–550 km, blue dots), and the overall ionosphere from 100 to 550 km (red dots). Radar-measured plasma density and temperature information as well as NRL-MSIS model neutral atmosphere parameters are used for conductance calculations.

In the  $F$  region, vertical and meridional winds as well as eastward electric field can all cause vertical ion drift. This fact means that it is impossible to distinguish the relative magnitudes of these two wind components from a  $V_z$  (or  $V_{\text{par}}$ ) measurement. The 50–100 m/s enhancement in  $V_z$  throughout the  $E$  and  $F$  regions carries an important signature of the atmospheric vertical upwelling. However, the magnitude of upwelling is not exactly known especially in the  $F$  region because the penetration electric field and meridional neutral wind effects do contribute to  $V_z$ . The  $F$  region ion upwelling is also possible at MHO with a  $67.5^\circ$  dip angle following the frictional heating to the ions, and it should also contribute to the observed 50–100 m/s  $V_z$  enhancement. For the  $E$  region, the ion upwelling only (without neutral upwelling) would be insufficient to account for the

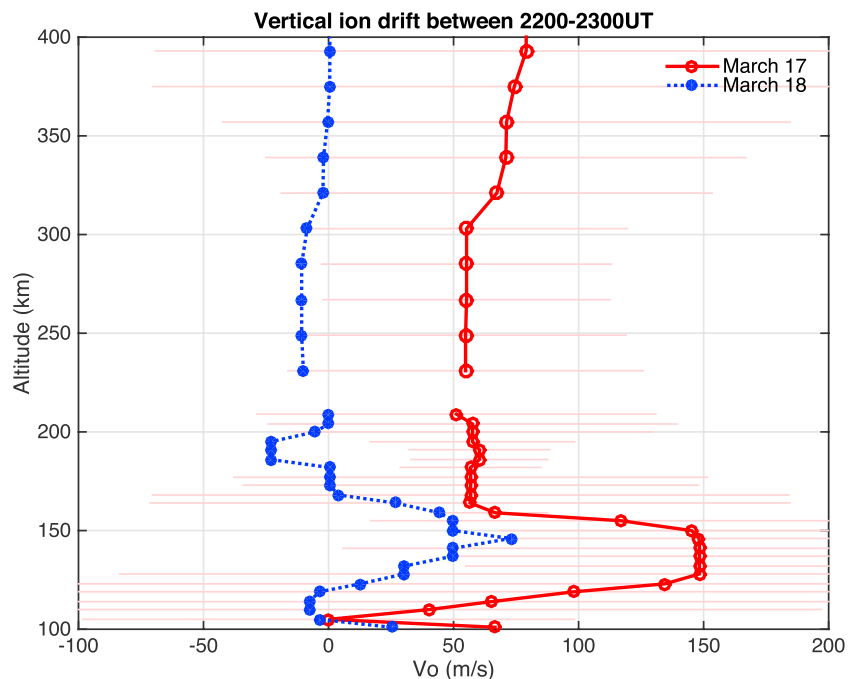


**Figure 14.** Average profiles of Millstone Hill vertical ion drift during 22–23 UT on 17 March (red) and 18 March (red), showing enhancement of the vertical drift throughout the  $E$  and  $F$  regions. The plot combines long-pulse waveform data for the  $F$  region and alternating code waveform data for the  $E$  and  $F_1$  regions.



large  $V_z$  change due to substantial ion-neutral collision rates. Nevertheless, the 50–100 m/s  $V_z$  enhancement of the ions within 1 h was substantial in the lower  $F$  region and  $E$  region if completely driven by neutral upwelling. The intensity of neutral upwelling must have been quite strong, producing adiabatic heating in this region where neutral temperature increases rapidly with height. This adiabatic heating effect could have appeared as an apparent cooling at certain heights. The ISR observations reported here could be examined in the future with a dedicated analysis (beyond the scope of this study) to resolve the ambiguity issue between ion composition and ion temperature in the  $F_1$  region ISR measurement.

Thermospheric upwelling at high latitudes is a well-known effect [e.g., Lühr *et al.*, 2004; Larsen and Meriwether, 2012]. Large vertical neutral winds may exist in the form of acoustic waves [Deng *et al.*, 2008]. But such a large upwelling has not been reported observationally to date for middle and subauroral latitudes, although upwelling of the neutral atmosphere caused by SAPS effects was simulated by Wang *et al.* [2012]. Simulation results further show that neutral composition changes, associated with upwelling of molecular rich air in subauroral and auroral regions, can become an important contributor to storm time deep and extended ionospheric electron density depletions at subauroral latitudes. Observational evidence of upwelling as reported here thus provides an additional and perhaps important causative factor for production of the midlatitude electron density trough that arrives immediately following the SED plume.

### 3.8. Ion Upflow/Outflow and Frictional Heating

The importance of frictional heating in the  $F$  region has been noted in a number of observational studies [Baron and Wand, 1983; Heelis and Coley, 1988] and simulations [Deng *et al.*, 2011]. When considering observed large amplitude ion drifts at subauroral latitudes, Buonsanto *et al.* [1992] also linked frictional effects to the production of ion upwelling and potentially outflow that can be a source of heavy cold ions for plasmaspheric and magnetospheric regions. Yeh and Foster [1990] reported a supersonic ion outflow speed at 800 km altitude during a great storm event with a maximum  $K_p$  of 9, and a speed of 400–500 m/s at 400 to 500 km altitude. Zhang *et al.* [2016] also indicated the correlation between the horizontal ion drift and the vertical ion drift at the DMSP satellite altitude in the polar cap, suggesting effects of frictional heating. In addition to frictional heating effects, the study also suggested that localized heating produced by precipitating  $O^+$  could account for observed ion outflows. Further research has concluded that  $O^+$  dynamics capable of accelerating heavy ions in the plasmasphere and magnetosphere most probably occurs in two steps: (1) ion upflow with thermal velocities below approximately 500 km and (2) ion outflow with suprathermal velocities at higher altitudes. Ion upflows below approximately 500 km may be caused by ion-neutral frictional heating or by soft particle precipitation [Strangeway *et al.*, 2005].

During the SAPS period for the 17 March 2015 study interval with maximum  $K_p$  of 7, a clear signature of ion outflow was present (Figure 15). The vertical ion drift (Figure 15a) had a very high speed of >400 m/s for a brief ~30 min period near ~22:43 UT at ~450 km over MHO, similar to that previously observed at MHO by Yeh and Foster [1990] during SAPS associated periods within the February 1986 great storm, and by Erickson *et al.* [2010] during the November 2004 storm. Vertical upward flux reached  $10^{13}$  ions  $m^{-2} s^{-1}$  at ~400 km and could have been larger at a higher altitude, similar to MHO earlier observations and somewhat smaller than results from some other SED events observed at DMSP altitudes [Yuan *et al.*, 2008]. During the 17 March 2015 upflow/outflow event,  $F$  region  $T_i$  was highly enhanced, and rapid acceleration in velocities occurred above 350 km, and these features imply that ion upwelling associated with frictional heating likely constituted a dominant source of plasma at low altitudes for subsequent outflow processes. However, the observed Millstone Hill electron temperature did not experience any substantial enhancement (not shown here;  $T_e$  values less than 2700 K below 450 km), unlike the Yeh and Foster [1990] case where  $T_e$  exceeded 4000 K at 450 km. A survey of DMSP energetic ion particle spectrograms (not shown) shows no sign of precipitating ions over the MHO latitude, as these typically occurred northward of SAPS. We therefore do not expect soft electron as well as ion precipitation to be present and consider it reasonable to speculate that a connection existed in this event between ion upflow/outflow and  $F$  region frictional heating.

### 3.9. $F_1$ Region Effects

During the 17 March 2015 20–24 UT SAPS period, the Millstone Hill electron density profile developed a clear  $F_1$  peak, and, in fact, the  $F_1$  peak density was often higher than the  $F_2$  peak seen in Figure 16 and known as a “G-condition” from ionosonde nomenclature [Buonsanto, 1999]. By contrast, quiet time daytime profiles (gray curves and black dashed line) show an  $F_2$  region electron density larger than the  $F_1$  region. Furthermore, prior to the SAPS influenced period (cyan curves and dotted line), the  $F_1$  ledge altitude was higher with a



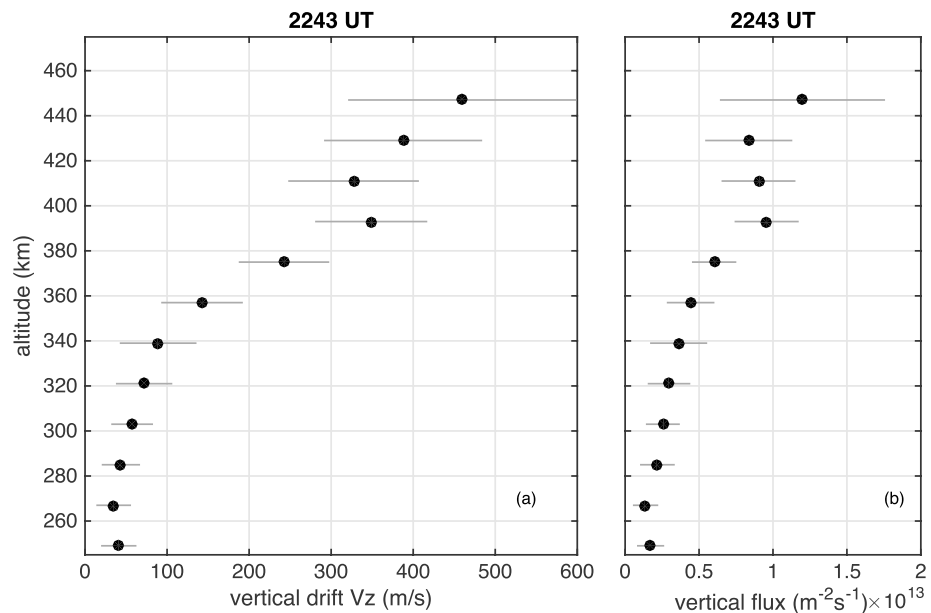


**Figure 15.** Millstone Hill height profiles of (a) vertical drift and (b) vertical flux at 22:43 UT on 17 March, showing a strong upward velocity of up to 400 m/s, and an upward flux of  $10^{13} \text{ m}^{-2} \text{ s}^{-1}$  at 450 km that are likely associated with ion outflows (see text).

larger associated density, but the  $F_2$  layer density remained larger than the  $F_1$  density. During typical sunset transition conditions, the  $F_1$  region electron density layer moves upward with an associated reduction in the  $F_1$  layer density, evolving the  $F_1$  peak into an  $F_1$  ledge or even causing a complete  $F_1$  disappearance [Zhang and Huang, 1995a]. The study of Zhang and Huang [1995b] suggested that  $F_1$  region transport assists in  $F_1$  peak formation. During the 17 March 2015 event, observations are therefore compatible with a scenario where, during SAPS hours, the ion upwelling discussed in the previous section likely moved plasma rich in molecular ions

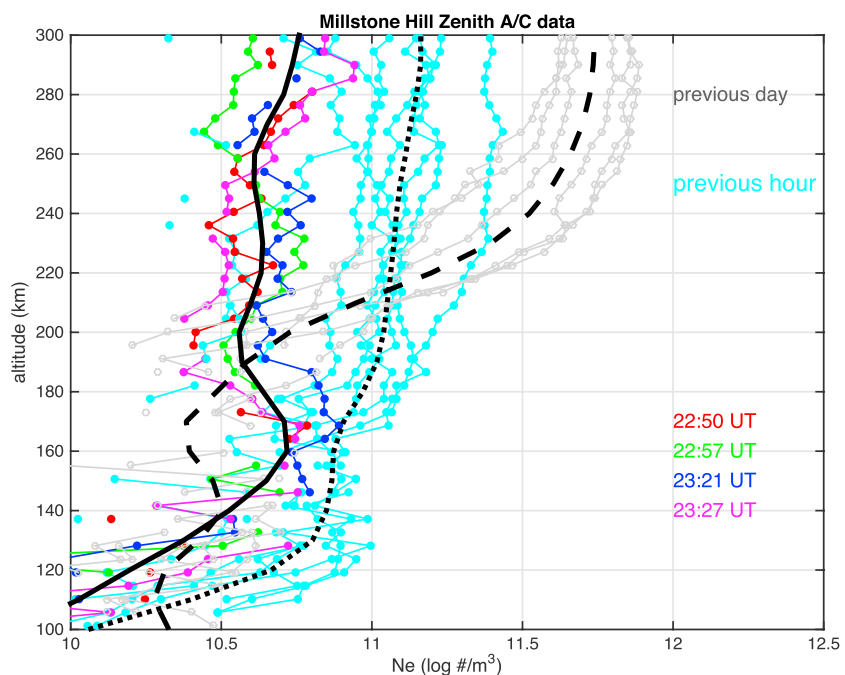


**Figure 16.** Profiles of Millstone Hill E and F regions electron density during the SAPS period on 17 March (red, green, blue, and magenta) and averages (solid, black), as well as profiles from the previous hour (cyan) and its average (dotted, black), and profiles of the same hours on the previous day (gray) and their average (long dashed line, black).

upward into the  $F_1$  region, while the  $F_2$  region electron density was simultaneously reduced due to elevated chemical recombination (section 3.5). The combination of these factors implies that at storm times, strong electrodynamic disturbance effects can ultimately produce  $F_1$  region electron density levels that surpass  $F_2$  region electron densities.

#### 4. Summary

The geomagnetic storm on 17–18 March 2015 was the largest to date in Solar Cycle 24 in terms of maximum negative  $Dst$  value and caused strong disturbances in ionosphere and thermosphere regions. At subauroral and midlatitudes, storm effects include fast ionospheric plasma drifts driven by SAPS processes and other associated ionospheric and thermospheric dynamics. This observational study has focused on ion-neutral coupling processes associated or correlated with significant electrodynamic forcing using incoherent scatter radars at Millstone Hill (MHO) and Arecibo (AO) along with DMSP in situ topside ionospheric data. During the main phase of the storm, in particular, in the afternoon and dusk sectors over North America, a number of ionospheric and thermospheric disturbance characteristics are identified and summarized schematically in Figure 17.

1. Both ground-based and in situ observations show fast plasma flows in the vicinity of Millstone Hill around 20–24 UT prior to dusk, with poleward/upward ion drifts also observed earlier in local noon and afternoon sectors.
2. A storm enhanced density (SED) plume passed over MHO in the afternoon sector when the ion drift was poleward/upward and subsequently moved westward. SAPS was located on the poleward edge of the plume. These effects are consistent with current understanding of the roles that large westward plasma drift and poleward/upward ion drift play in forming and evolving SED plumes.
3. Prompt penetration electric field (i.e., poleward ion drift) was observed in MHO poleward/upward ion drift associated with the SED and was also seen at ~22 UT over MHO and AO, in a manner consistent with DMSP vertical drift data.
4. Meridional neutral winds surged equatorward on the dayside at MHO, followed by oscillations with a 2–3 h period at both MHO and AO.
5. Oscillations in the meridional ion drift perpendicular to the field line (zonal electric field) accompanied oscillations in the meridional wind at AO. The well-known anticorrelation between the parallel ion drift and the ion drift perpendicular to the field line shown in AO data was likely related to a storm time polarization electric field generated by large scale TADs.
6. MHO ion temperature and vertical ion drift enhancements in the  $E$  and  $F$  regions were observed during the SAPS period. The strong upward ion drifts of over 50 m/s from the  $E$  region into the  $F$  region represented the ionospheric manifestation of neutral wind upwelling driven by frictional heating which is presumably associated with the SAPS type of large ionospheric drift.
7. An ion upflow/upwelling event was observed briefly at 22:43 UT over Millstone Hill, in the middle of the SAPS time period with presumably strong frictional heating present throughout the ionospheric  $E$  and  $F$  regions. The ion upflow/upwelling was seen as an upward vertical ion drift increase up to ~400 m/s magnitude and an upward flux close to  $10^{13}$  ions/m<sup>2</sup> s.
8. Storm time ionospheric  $F_1$  region subauroral electron density can at times be larger than  $F_2$  region electron density during SAPS periods, due to the reduction in  $F$  region electron density shortly before arrival of the midlatitude trough as well as increases in the  $F_1$  region molecular ion density as a result of ion upwelling.

The 17 March 2015 storm highlighted several significant ion-neutral coupling processes, present in some cases nearly simultaneously over a several hour span and which happened here during a single event. These processes, and their associated ionospheric and thermospheric variations, considerably expand and refine our picture of storm time subauroral and midlatitude ionosphere and thermosphere changes. In particular, during storm main phase, subauroral and/or midlatitude strong plasma flow convect ionospheric plasma westward from the nightside to dayside. Simultaneously, penetration electric fields can provide upward and poleward plasma drifts, moving dayside plasma to high altitudes (where chemical loss rate of the ions is slow) and also injecting material at high latitudes near throat/polar cap entry regions in a manner that shapes SED formation and evolution. Strong SAPS region ion-neutral relative motion in the horizontal direction can also produce frictional heating not only in ionospheric but also thermospheric material. Neutral upwelling presumably associated with these features drives substantial ionospheric ion vertical drifts throughout the  $E$  and  $F$  regions, with potentially large impacts on thermospheric composition locally and remotely. We also

# Acknowledgments

S.R.Z., P.J.E., Y.Z., W.W., and C.H. acknowledge NASA LWS funding support (NNX15AB83G). S.R.Z.'s effort is also partially funded by the DoD Multidisciplinary Research Program of the University Research Initiative (MURI) project ONR15-FOA-0011. Ground-based observational data from the incoherent scatter radars and FPIs at both Millstone Hill and Arecibo are obtained through the Madrigal database system ([www.openmadrigal.org](http://www.openmadrigal.org)) developed and maintained by MIT Haystack Observatory. *Dst* data are obtained from the World Data Center at Kyoto University (<http://wdc.kugi.kyoto-u.ac.jp/wdc/Sec3.html>). The solar wind data are obtained from the Advanced Composition Explorer (ACE) satellite, and the real-time 1 h average IMF  $B_z$  data sets are obtained from the archive at the NOAA Space Weather Prediction Center ([ftp://ftp.swpc.noaa.gov/pub/lists/ace2/](http://ftp.swpc.noaa.gov/pub/lists/ace2/)). Other data used in this study were obtained from the Madrigal database system. ISR observations and analysis at MIT Haystack Observatory are supported by cooperative agreement AGS-1242204 between the National Science Foundation and the Massachusetts Institute of Technology. ISR observations at Arecibo Observatory are supported by cooperative agreement AST-1160876 between the National Science Foundation and SRI International. GPS TEC data products and access through the Madrigal distributed data system are provided to the community by the Massachusetts Institute of Technology under support from U.S. National Science Foundation grant AGS-1242204. Data for the TEC processing are provided from the following organizations: UNAVCO, Scripps Orbit and Permanent Array Center, Institut Geographique National, France, International GNSS Service, The Crustal Dynamics Data Information System (CDDIS), National Geodetic Survey, Instituto Brasileiro de Geografia e Estatística, RAMSAC CORS of Instituto Geográfico Nacional del la República Argentina, Arecibo Observatory, Low-Latitude Ionospheric Sensor Network (LISN), Topcon Positioning Systems, Inc., Canadian High Arctic Ionospheric Network, Institute of Geology and Geophysics (Chinese Academy of Sciences), China Meteorology Administration, Centro di Ricerche Sismologiche, Systeme d'Observation du Niveau des Eaux Littorales (SONEL), RENAG : REseau NAtional GPS permanent, and GeoNet—the official source of geological hazard information for New Zealand.

## Storm-time Subauroral Dynamics

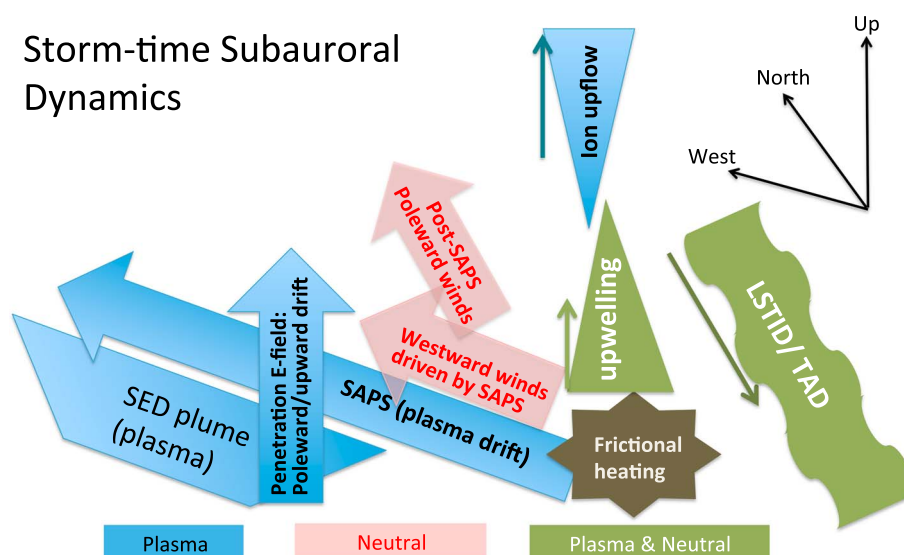


**Figure 17.** Schematic summary representation of primary storm time subauroral ionosphere and thermosphere dynamics observed during the 17–18 March 2015 St. Patrick's Day great geomagnetic storm.

speculate that strong ion upwellings/upflow (providing potential ion outflow sources) can be associated with SAPS related ion-neutral processes. Storm time neutral wind disturbances are of significant amplitude, manifesting as a dayside equatorward surge at subauroral/midlatitudes and oscillating TADs into low latitudes during the main phase of the storm, accompanied by an abnormal nightside poleward surge. Observed storm time TAD at low latitudes are strongly correlated to oscillating (zonal) electric field.

These features raise the interesting question for future study of whether the source region of these neutral disturbances is always in the auroral zone as traditionally anticipated, or whether SAPS regions can under certain conditions provide strong frictional heating that ultimately becomes another significant source of storm time disturbances.

## References

- Astafyeva, E., I. Zakharenkova, and M. Förster (2015), Ionospheric response to the 2015 St. Patrick's Day storm: A global multi-instrumental overview, *J. Geophys. Res. Space Physics*, **120**, 9023–9037, doi:10.1002/2015JA021629.
- Basu, S., S. Basu, F. J. Rich, K. M. Groves, E. MacKenzie, C. Coker, Y. Sahai, P. R. Fagundes, and F. Becker-Guedes (2007), Response of the equatorial ionosphere at dusk to penetration electric fields during intense magnetic storms, *J. Geophys. Res.*, **112**, A08308, doi:10.1029/2006JA012192.
- Baron, M. J., and R. H. Wand (1983), F region ion temperature enhancements resulting from Joule heating, *J. Geophys. Res.*, **88**(A5), 4114–4118, doi:10.1029/JA088iA05p04114.
- Blanc, M., and A. D. Richmond (1980), The ionospheric disturbance dynamo, *J. Geophys. Res.*, **85**, 1669–1686.
- Behnke, R. A., and R. M. Harper (1973), Vector measurements of F region ion transport at Arecibo, *J. Geophys. Res.*, **78**(34), 8222–8234, doi:10.1029/JA078i034p08222.
- Brekke, A., and Y. Kamide (1996), On the relationship between Joule and frictional heating in the polar ionosphere, *J. Atmos. Terr. Phys.*, **58**(1–4), 139–143.
- Burnside, R. G., C. A. Tepley, and V. B. Wickwar (1987), The  $O^+ - O$  collision cross-section: Can it be inferred from aeronomical measurements?, *Ann. Geophys.*, **5A**, 343–349.
- Buonsanto, M. J. (1999), Ionospheric storms — A review, *Space Sci. Rev.*, **88**, 563–601.
- Buonsanto, M. J., J. C. Foster, and D. P. Sipler (1992), Observations from Millstone Hill during the geomagnetic disturbances of March and April 1990, *J. Geophys. Res.*, **97**(A2), 1225–1243, doi:10.1029/91JA02428.
- Buonsanto, M. J., and J. C. Foster (1993), Effects of magnetospheric electric fields and neutral winds on the low-middle latitude ionosphere during the March 20–21, 1990, storm, *J. Geophys. Res.*, **98**(A11), 19,133–19,140, doi:10.1029/93JA01807.
- Dalgarno, A. (1964), Ambipolar diffusion in the F-region, *J. Atmos. Terr. Phys.*, **26**, 939–939.
- Deng, Y., A. D. Richmond, A. J. Ridley, and H.-L. Liu (2008), Assessment of the non-hydrostatic effect on the upper atmosphere using a general circulation model (GCM), *Geophys. Res. Lett.*, **35**, L01104, doi:10.1029/2007GL032182.
- Deng, Y., T. J. Fuller-Rowell, R. A. Akmaev, and A. J. Ridley (2011), Impact of the altitudinal Joule heating distribution on the thermosphere, *J. Geophys. Res.*, **116**, A05313, doi:10.1029/2010JA016019.
- Drob, D. P., et al. (2008), An empirical model of the Earth's horizontal wind fields: HWM07, *J. Geophys. Res.*, **113**, A12304, doi:10.1029/2008JA013668.
- Emmert, J. T., et al. (2008), DWM07 global empirical model of upper thermospheric storm-induced disturbance winds, *J. Geophys. Res.*, **113**, A11319, doi:10.1029/2008JA013541.
- Erickson, P. J., L. P. Goncharenko, M. J. Nicolls, M. Ruohoniemi, and M. C. Kelley (2010), Dynamics of North American sector ionospheric and thermospheric response during the November 2004 superstorm, *J. Atmos. Sol. Terr. Phys.*, **72**(4), 292–301.

- Erickson, P. J., F. Beroz, and M. Z. Miskin (2011), Statistical characterization of the American sector subauroral polarization stream using incoherent scatter radar, *J. Geophys. Res.*, **116**, A00J21, doi:10.1029/2010JA015738.
- Fejer, B. G., C. A. Gonzales, D. T. Farley, M. C. Kelley, and R. F. Woodman (1979), Equatorial electric fields during magnetically disturbed conditions. 1. The effect of the interplanetary magnetic field, *J. Geophys. Res.*, **84**, 5797–5802.
- Foster, J. C. (1993), Storm time plasma transport at middle and high latitudes, *J. Geophys. Res.*, **98**(A2), 1675–1689, doi:10.1029/92JA02032.
- Foster, J. C., and W. J. Burke (2002), SAPS: A new categorization for sub-auroral electric fields, *Eos Trans. AGU*, **83**(36), 393–394, doi:10.1029/2002EO000289.
- Foster, J. C., and H. B. Vo (2002), Average characteristics and activity dependence of the subauroral polarization stream, *J. Geophys. Res.*, **107**(A12), 1475, doi:10.1029/2002JA009409.
- Foster, J. C., W. Rideout, B. Sandel, W. T. Forrester, and F. J. Rich (2007), On the relationship of SAPS to storm-enhanced density, *J. Atmos. Sol. Terr. Phys.*, **69**(3), 303–313.
- Foster, J. C., et al. (2005), Multiradar observations of the polar tongue of ionization, *J. Geophys. Res.*, **110**, A09S31, doi:10.1029/2004JA010928.
- Galperin, Y., Y. N. Ponomarev, and A. G. Zosimova (1974), Plasma convection in the polar ionosphere, *Ann. Geophys.*, **30**, 1–7.
- Goncharenko, L. P., J. C. Foster, A. J. Coster, C. Huang, N. Aponte, and L. J. Paxton (2007), Observations of a positive storm phase on September 10, 2005, *J. Atmos. Sol. Terr. Phys.*, **69**, 1253–1272.
- Hairston, M., W. R. Coley, and R. Stoneback (2016), Responses in the polar and equatorial ionosphere to the March 2015 St. Patrick Day storm, *J. Geophys. Res. Space Physics*, **121**, 11,213–11,234, doi:10.1002/2016JA023165.
- Heelis, R. A. (2008), Low- and middle-latitude ionospheric dynamics associated with magnetic storms, in *Midlatitude Ionospheric Dynamics and Disturbances*, edited by P. M. Kintner et al., pp. 51–61, AGU, Washington, D. C., doi:10.1029/181GM06.
- Heelis, R. A., and W. R. Coley (1988), Global and local Joule heating effects seen by DE 2, *J. Geophys. Res.*, **93**(A7), 7551–7557, doi:10.1029/JA093iA07p07551.
- Huang, C., I. Sazykin, R. Spiro, J. Goldstein, G. Crowley, and J. M. Ruohoniemi (2006), Storm-time penetration electric fields and their effects, *Eos Trans. AGU*, **87**(13), 131–131, doi:10.1029/2006EO130005.
- Huang, C.-S. (2016), Plasma drifts and polarization electric fields associated with TID-like disturbances in the low-latitude ionosphere: C/NOFS observations, *J. Geophys. Res. Space Physics*, **121**, 1802–1812, doi:10.1002/2015JA022201.
- Kataoka, R., D. Shiota, E. Kilpua, and K. Keika (2015), Pileup accident hypothesis of magnetic storm on 17 March 2015, *Geophys. Res. Lett.*, **42**, 5155–5161, doi:10.1002/2015GL064816.
- Kelley, M. C., J. J. Makela, J. L. Chau, and M. J. Nicolls (2003), Penetration of the solar wind electric field into the magnetosphere/ionosphere system, *Geophys. Res. Lett.*, **30**(4), 1158, doi:10.1029/2002GL016321.
- Kirchengast, G., K. Hocke, and K. Schlegel (1996), The gravity wave-TID relationship: Insight via theoretical model-EISCAT data comparison, *J. Atmos. Terr. Phys.*, **58**(1–4), 233–243.
- Larsen, M. F., and J. W. Meriwether (2012), Vertical winds in the thermosphere, *J. Geophys. Res.*, **117**, A09319, doi:10.1029/2012JA017843.
- Lehtinen, M. S., and I. Häggström (1987), A new modulation principle for incoherent scatter measurements, *Radio Sci.*, **22**(4), 625–634, doi:10.1029/R502i004p00625.
- Liu, J., W. Wang, A. Burns, X. Yue, S. Zhang, Y. Zhang, and C. Huang (2016), Profiles of ionospheric storm-enhanced density during the 17 March 2015 great storm, *J. Geophys. Res. Space Physics*, **121**, 727–744, doi:10.1002/2015JA021832.
- Lu, G., L. P. Goncharenko, A. D. Richmond, R. G. Roble, and N. Aponte (2008), A dayside ionospheric positive storm phase driven by neutral winds, *J. Geophys. Res.*, **113**, A08304, doi:10.1029/2007JA012895.
- Lühr, H., M. Rother, W. Köhler, P. Ritter, and L. Grunwaldt (2004), Thermospheric up-welling in the cusp region: Evidence from CHAMP observations, *Geophys. Res. Lett.*, **31**, L06805, doi:10.1029/2003GL019314.
- Maruyama, N., A. D. Richmond, T. J. Fuller-Rowell, M. V. Codrescu, S. Sazykin, F. R. Toffoletto, R. W. Spiro, and G. H. Millward (2005), Interaction between direct penetration and disturbance dynamo electric fields in the storm-time equatorial ionosphere, *Geophys. Res. Lett.*, **32**, L17105, doi:10.1029/2005GL023763.
- Mendillo, M. (2006), Storms in the ionosphere: Patterns and processes for total electron content, *Rev. Geophys.*, **44**, RG4001, doi:10.1029/2005RG000193.
- Nishida, A. (1968), Coherence of geomagnetic DP2 fluctuations with interplanetary magnetic variations, *J. Geophys. Res.*, **76**, 5549–5559.
- Nava, B., J. Rodríguez-Zuluaga, K. Alazo-Cuartas, A. Kashcheyev, Y. Migoya-Orué, S. M. Radicella, C. Amory-Mazaudier, and R. Fleury (2016), Middle- and low-latitude ionosphere response to 2015 St. Patrick's Day geomagnetic storm, *J. Geophys. Res. Space Physics*, **121**, 3421–3438, doi:10.1002/2015JA022299.
- Pesnell, W. D., K. Omidvar, and W. R. Hoegy (1993), Momentum transfer collision frequency of  $O^+ - O$ , *Geophys. Res. Lett.*, **20**, 1343–1346.
- Picone, J. M., A. E. Hedin, D. P. Drob, and A. C. Aikin (2002), NRLMSISE-00 empirical model of the atmosphere: Statistical comparisons and scientific issues, *J. Geophys. Res.*, **107**(A12), 1468, doi:10.1029/2002JA009430.
- Rideout, W., and A. Coster (2006), Automated GPS processing for global total electron content data, *GPS Solutions*, **10**(3), 219–228.
- Rishbeth, H., S. Ganguly, and J. C. G. Walker (1978), Field-aligned and field-perpendicular velocities in the ionospheric F2-layer, *J. Atmos. Terr. Phys.*, **40**, 767–784.
- Salah, J. E., and J. M. Holt (1974), Midlatitude thermospheric winds from incoherent scatter radar and theory, *Radio Sci.*, **9**(2), 301–313, doi:10.1029/R5009i002p00301.
- Schunk, R. W., and A. F. Nagy (2000), *Ionospheres*, Cambridge Univ. Press, New York.
- Strangeway, R. J., R. E. Ergun, Y. J. Su, C. W. Carlson, and R. C. Elphic (2005), Factors controlling ionospheric outflows as observed at intermediate altitudes, *J. Geophys. Res.*, **110**, A03221, doi:10.1029/2004JA010829.
- Otsuka, Y., K. Shiokawa, T. Ogawa, and P. Wilkinson (2004), Geomagnetic conjugate observations of medium-scale traveling ionospheric disturbances at midlatitude using all-sky airglow imagers, *Geophys. Res. Lett.*, **31**, L15803, doi:10.1029/2004GL020262.
- Saito, A., T. Iyemori, M. Sugiura, N. C. Maynard, T. L. Aggson, L. H. Brace, M. Takeda, and M. Yamamoto (1995), Conjugate occurrence of the electric field fluctuations in the nighttime midlatitude ionosphere, *J. Geophys. Res.*, **100**, 21,439–21,452, doi:10.1029/95JA01505.
- Shiokawa, K., Y. Otsuka, T. Ogawa, N. Balan, K. Igarashi, A. J. Ridley, D. J. Knipp, A. Saito, and K. Yumoto (2002), A large-scale traveling ionospheric disturbance during the magnetic storm of 15 September 1999, *J. Geophys. Res.*, **107**(A6), 1088, doi:10.1029/2001JA000245.
- Shiokawa, K., et al. (2003), Thermospheric wind during a storm-time large-scale traveling ionospheric disturbance, *J. Geophys. Res.*, **108**(A12), 1423, doi:10.1029/2003JA010001.
- Spiro, R. W., R. A. Heelis, and W. B. Hanson (1979), Rapid subauroral ion drifts observed by Atmosphere Explorer C, *Geophys. Res. Lett.*, **6**, 657–660, doi:10.1029/GL006i008p00657.
- Sulzer, M. P. (1986), A radar technique for high range resolution incoherent scatter autocorrelation function measurements utilizing the full average power of klystron radars, *Radio Sci.*, **21**(6), 1033–1040, doi:10.1029/R502i006p01033.

- Tsurutani, B., et al. (2004), Global dayside ionospheric uplift and enhancement associated with interplanetary electric fields, *J. Geophys. Res.*, **109**, A08302, doi:10.1029/2003JA010342.
- Tulasi Ram, S., et al. (2016), Duskside enhancement of equatorial zonal electric field response to convection electric fields during the St. Patrick's Day storm on 17 March 2015, *J. Geophys. Res. Space Physics*, **121**, 538–548, doi:10.1002/2015JA021932.
- Vierinen, J., A. J. Coster, W. C. Rideout, P. J. Erickson, and J. Norberg (2016), Statistical framework for estimating GNSS bias, *Atmos. Meas. Tech.*, **9**, 1303–1312, doi:10.5194/amt-9-1303-2016.
- Walker, J. (1980), Correlation of wind and electric field in the nocturnal F-region, *Geophys. J. R. Astron. Soc.*, **60**(1), 85–93.
- Wang, H., H. Lüher, K. Häusler, and P. Ritter (2011), Effect of subauroral polarization streams on the thermosphere: A statistical study, *J. Geophys. Res.*, **116**, A03312, doi:10.1029/2010JA016236.
- Wang, W., E. R. Talaat, A. G. Burns, B. Emery, S.-Y. Hsieh, J. Lei, and J. Xu (2012), Thermosphere and ionosphere response to subauroral polarization streams (SAPS): Model simulations, *J. Geophys. Res.*, **117**, A07301, doi:10.1029/2012JA017656.
- Yeh, H. C., and J. C. Foster (1990), Storm time heavy ion outflow at mid-latitude, *J. Geophys. Res.*, **95**(A6), 7881–7891.
- Yeh, H.-C., J. C. Foster, F. J. Rich, and W. Swider (1991), Storm time electric field penetration observed at mid-latitude, *J. Geophys. Res.*, **96**(A4), 5707–5721, doi:10.1029/90JA02751.
- Yuan, Z.-G., X.-H. Deng, and J.-F. Wang (2008), DMSP/GPS observations of intense ion upflow in the midnight polar ionosphere associated with the SED plume during a super geomagnetic storm, *Geophys. Res. Lett.*, **35**, L19110, doi:10.1029/2008GL035462.
- Yuan, Z.-G., X.-H. Deng, S.-R. Zhang, W.-X. Wan, and B. W. Reinisch (2009), F region behavior in the SED plume during a geomagnetic superstorm: A case study, *J. Geophys. Res.*, **114**, A08303, doi:10.1029/2008JA013841.
- Zhang, S.-R., and J. M. Holt (2007), Ionospheric Climatology and Variability from Long-term and Multiple Incoherent Scatter Radar Observations: Climatology in Eastern American Sector, *J. Geophys. Res.*, **112**, A06328, doi:10.1029/2006JA012206.
- Zhang, S.-R., and X.-Y. Huang (1995a), An ionospheric numerical model and some results for the electron density structure below the  $F_2$  peak, *Adv. Space Res.*, **16**(1), 119–120.
- Zhang, S.-R., and X.-Y. Huang (1995b), A numerical study of ionospheric profiles for mid-latitudes, *Ann. Geophys.*, **13**(5), 551–557.
- Zhang, S.-R., J. M. Holt, and M. McRae (2007), High latitude convection model based on long-term incoherent scatter radar observations in North America, *J. Atmos. Sol. Terr. Phys.*, **69**, 1273–1291, doi:10.1016/j.jastp.2006.08.017.
- Zhang, S.-R., et al. (2015), Thermospheric poleward wind surge at midlatitudes during great storm intervals, *Geophys. Res. Lett.*, **42**, 5132–5140, doi:10.1002/2015GL064836.
- Zhang, Q.-H., et al. (2016), Earth's ion upflow associated with polar cap patches: Global and in situ observations, *Geophys. Res. Lett.*, **43**, 1845–1853, doi:10.1002/2016GL067897.
- Zou, S., M. B. Moldwin, A. J. Ridley, M. J. Nicolls, A. J. Coster, E. G. Thomas, and J. M. Ruohoniemi (2014), On the generation/decay of the storm-enhanced density plumes: Role of the convection flow and field-aligned ion flow, *J. Geophys. Res. Space Physics*, **119**, 8543–8559, doi:10.1002/2014JA020408.